



ELSEVIER

Contents lists available at ScienceDirect

# Quaternary Science Reviews

journal homepage: [www.elsevier.com/locate/quascirev](http://www.elsevier.com/locate/quascirev)

Invited paper

## Intensified organic carbon burial on the Australian shelf after the Middle Pleistocene transition

Gerald Auer<sup>a, b, \*</sup>, Benjamin Petrick<sup>c, d</sup>, Toshihiro Yoshimura<sup>b</sup>, Briony L. Mamo<sup>e</sup>, Lars Reuning<sup>d</sup>, Hideko Takayanagi<sup>f</sup>, David De Vleeschouwer<sup>g</sup>, Alfredo Martinez-Garcia<sup>c</sup>

<sup>a</sup> University of Graz, Institute of Earth Sciences (Geology and Paleontology), NAWI Graz Geocenter, Heinrichstraße 26, 8010, Graz, Austria

<sup>b</sup> Research Institute for Marine Resources Utilization (Biogeochemistry Research Center), Japan Agency for Marine-Earth Science and Technology (JAMSTEC), 2-15 Natsushima-cho, Yokosuka, Kanagawa, 237-0061, Japan

<sup>c</sup> Max Planck Institute for Chemistry, Climate Geochemistry Department, Hahn-Meitner-Weg 1, 55128, Mainz, Germany

<sup>d</sup> Kiel University, Institute for Geosciences, Ludewig-Meyn-Str. 10, 24118, Kiel, Germany

<sup>e</sup> Macquarie University, Department of Biological Sciences, North Ryde, 2109, NSW, Australia

<sup>f</sup> Institute of Geology and Paleontology, Tohoku University, Aobayama, Sendai, 980-8578, Japan

<sup>g</sup> MARUM-Center for Marine and Environmental Sciences, Klagenfurterstraße 2-4, Bremen, 28359, Germany

### ARTICLE INFO

#### Article history:

Received 25 September 2020

Received in revised form

19 April 2021

Accepted 19 April 2021

Available online xxx

Handling Editor: A. Voelker

#### Keywords:

Middle pleistocene transition

Calcareous nannoplankton

Primary productivity

Organic carbon burial

Leeuwin current

### ABSTRACT

The Middle Pleistocene Transition (MPT) represents a major change in Earth's climate state, exemplified by the switch from obliquity-dominated to ~100-kyr glacial/interglacial cycles. To date, the causes of this significant change in Earth's climatic response to orbital forcing are not fully understood. Nonetheless, this transition represents an intrinsic shift in Earth's response to orbital forcing, without fundamental changes in the astronomical rhythms. This study presents new high-resolution records of International Ocean Discovery Program (IODP) Site U1460 (eastern Indian Ocean, 27°S), including shallow marine productivity and organic matter flux reconstructions. The proxy series covers the interval between 1.1 and 0.6 Ma and provides insights into Pleistocene Leeuwin Current dynamics along the West Australian shelf. The large >45 m global sea level drop during the marine isotope stage (MIS) 22–24 is marked in our data, suggesting that the MPT led to large-scale changes in Indian Ocean circulation patterns and surface water conditions. We consider shelf exposure (and thus the “Sahul-Indian Ocean Bjerknes mechanism”) as a possible key process to increase the upwelling of nutrient-rich sub-Antarctic Mode waters through the Leeuwin Undercurrent along the Australian shelf. We conclude that the shoaling of nutrient-rich lower-thermocline waters enhanced mid-latitude productivity patterns in the eastern Indian Ocean across the 900-ka event.

© 2021 The Author(s). Published by Elsevier Ltd. This is an open access article under the CC BY-NC-ND license (<http://creativecommons.org/licenses/by-nc-nd/4.0/>).

### 1. Introduction

The Middle Pleistocene Transition (MPT), also called the Early-Middle Pleistocene Transition (EMPT), represents a fundamental reorganization of the Earth's climatic state (Bajo et al., 2020; Clark et al., 2006; Crucifix et al., 2006; Feng and Bailer-Jones, 2015; Hasenfratz et al., 2019; Head and Gibbard, 2015; Huybers and Wunsch, 2005; Kemp et al., 2010; Kender et al., 2016; Kunkelova et al., 2018; Lisiecki and Raymo, 2005; Maslin and Brierley, 2015; McClymont and Rosell-Melé, 2005; Pena and Goldstein, 2014;

Robinson et al., 2019). This climatic reorganization occurs together with a pronounced shift from Pliocene and Early Pleistocene glacial-interglacial (G-IG) cycles that follow 41-kyr obliquity forcing towards the quasi-periodic 100-kyr G-IG cycles that dominated the last ~1 million years of the Earth's climatic history (Chalk et al., 2017; Clark et al., 2006; Elderfield et al., 2012; Ford et al., 2016; Head and Gibbard, 2015; Kender et al., 2018; Maslin and Brierley, 2015; McClymont et al., 2013). In terms of waveforms, the MPT represents a shift from sinusoidal 41-kyr cycles towards sharp, saw-tooth-like ~100-kyr cycles whose shape is marked by large and rapid deglaciations (e.g., Maslin and Brierley, 2015). The effect of the MPT is well represented in paleoclimatological proxy records, such as sea surface temperatures (SSTs) and deep ocean  $\delta^{18}\text{O}$  records between 1.2 and 0.6 Myr ago, that indicate global cooling and

\* Corresponding author. University of Graz, Institute of Earth Sciences (Geology and Paleontology), NAWI Graz Geocenter, Heinrichstraße 26, 8010, Graz, Austria.  
E-mail address: [gerald.auer@uni-graz.at](mailto:gerald.auer@uni-graz.at) (G. Auer).

glacial lengthening (Head and Gibbard, 2015; Kender et al., 2016; Kunkelova et al., 2018; Maslin and Brierley, 2015; McClymont and Rosell-Melé, 2005). The switch in dominant climatic pacing is, however, also often attributed to a single pronounced event occurring ~900 ka ago termed the 900-ka event (Clark et al., 2006; Kemp et al., 2010; Maslin and Brierley, 2015; Robinson et al., 2019). The 900-ka event corresponds to marine isotope stages (MIS) 24 and 22 separated by a weak or 'failed' interglacial MIS 23 (Clark et al., 2006).

The mid- and low-latitude shelf areas' response to the major climate reorganization that occurred during the MPT is poorly constrained. Shallow marine productivity and thus organic matter fluxes on shelf areas are expected to be higher during interglacials, although they are quickly recycled and become again available in the upper water column. During glacial sea level drops, increased shelf exposure limits shallow benthic denitrification (Ren et al., 2017). Reduced organic matter recycling could, in turn, lead to higher total organic carbon (TOC) accumulation in shallow marine areas of the ocean, especially in low to mid-latitudes. Substantial sea level drops (>45 m) occurred for the first time in several million years during the 900-ka event (Elderfield et al., 2012). Changes in the nutrient cycling in the Southern Ocean (SO) may also have impacted nutrient supply via sub-Antarctic mode water (SAMW) formation within the northern branch of the Antarctic divergence north of the Antarctic circumpolar current (ACC), where today a large portion of intermediate water nutrients are subducted (Laufkötter and Gruber, 2018; Moore et al., 2018; Sarmiento et al., 2004). The northward expansion of SO frontal systems across the MPT (Kemp et al., 2010; Martínez-García et al., 2010) could have increased SO nutrient transport towards the western Australian coast. However, this process could have been counteracted by higher glacial productivity and nutrient consumption driven by iron fertilization in the Subantarctic Zone of the SO (Martínez García et al., 2009, 2011).

To test these potential links, we investigated a set of multi-proxy records, including calcareous nannofossil accumulation rates, TOC, uranium content, and mass accumulation rates (MARs) combined with low-resolution C<sub>37</sub> alkenone MARs in the shallow marine International Ocean Discovery Program (IODP) Site U1460. Site U1460 was drilled during IODP Expedition 356 (Gallagher et al., 2017) and is situated on the southwest shelf offshore Western Australia, within the path of the southward flowing Leeuwin Current (LC), and bathed within the waters of the Leeuwin Undercurrent (LUC; Fig. 1). In the present study, we aim to elucidate the influence of Early to Middle Pleistocene changes in G-IG patterns on the LC and LUC system. These data provide the opportunity to evaluate changes in low and mid-latitude productivity and organic matter fluxes. We relate these changes to the evolution of SAMW formation and transport (via the LUC) and Indonesian Throughflow (ITF) dynamics through the LC during the MPT when higher amplitude 100-kyr G-IG cycles became dominant. These local environmental changes are then brought into the context with high-resolution sea level reconstructions from Ocean Drilling Program (ODP) Site 1123 offshore New Zealand (Elderfield et al., 2012) and the influence of orbital forcing on organic matter fluxes at the mid-latitudes in the Indian Ocean.

The results are then linked to regional and global patterns observed in existing data from previous drilling campaigns in the southern Indo-Pacific region. Thereby we define how interactions of G-IG changes in sea level, ITF connectivity, SAMW, and changing southern hemisphere wind patterns affected conditions along the southwest shelf of Australia (Fig. 1; Gallagher et al., 2017). Finally, we explore the link between changes in the global ocean circulation patterns during the MPT with the expression of local benthic communities and link these to potential changes in the LUC.

Thereby we investigate how southern hemisphere high-latitude processes (Farmer et al., 2019; Ford et al., 2016; Koch-Larrouy et al., 2010; Pena and Goldstein, 2014; Ronge et al., 2015) affected the formation and influx of cool, ventilated low salinity SAMW into the eastern Indian Ocean via the Flinders Current (Bull and Seville, 2016; Koch-Larrouy et al., 2010; Ridgway and Dunn, 2007; van Seville et al., 2014; Speich et al., 2007) and how it may be related to changes in shelf primary productivity during and after the MPT.

## 2. Oceanographic setting

### 2.1. Surface oceanography

The LC represents the only southward flowing eastern boundary current in the Southern Hemisphere (Wijeratne et al., 2018, Fig. 1a). The LC waters are sourced directly from the ITF and flow along a steric height gradient from the West Australian shelf towards the Southwest Cape of Australia (Domingues et al., 2007; Furue et al., 2013; Okada and Wells, 1997; Wijeratne et al., 2018). The LC is a warm oligotrophic current that suppresses wind-driven upwelling and pelagic productivity along the western Australian margin. There is, however, evidence that kinematic mixing through eddies and meanders of the LC (Fig. 1b) results in increased phytoplankton activity during times of maximum LC strength in Autumn and Winter (Feng et al., 2009; Koslow et al., 2008; Rousseaux et al., 2012; Thompson et al., 2011; Waite et al., 2007a). The LC then rounds the Southwest Cape flowing eastward south of Australia (Furue et al., 2017; Wijeratne et al., 2018). South of Australia, the LC waters intermix with Pacific waters from the Tasman Sea, including the Tasman Leakage (TL) and northward-flowing Antarctic surface waters (Sloyan and Rintoul, 2001; Koch-Larrouy et al., 2010). These waters are subsequently subducted and ventilated in this region within the deep winter mixed layers north of the sub-Antarctic front (SAF) as SAMW (Koch-Larrouy et al., 2010; Richardson et al., 2019; Rosell-Fieschi et al., 2013).

### 2.2. Subsurface oceanography

Today SAMW formation south of Australia occurs along a narrow band along the southern tip of Western Australia and the subtropical front between 35°S and 40°S that constitutes an important formation region for Indian Ocean SAMW (Fine, 1993; Koch-Larrouy et al., 2010; Richardson et al., 2019). The SAMW formed south of Australia also incorporates AAIW (Koch-Larrouy et al., 2010) entering the Indian Ocean via the TL south of Australia (Richardson et al., 2019; Ridgway and Dunn, 2007; Rosell-Fieschi et al., 2013; Speich et al., 2002; van Seville et al., 2014).

After sinking to intermediate water depths, these newly formed SAMW again flow westward within the Flinders current (Bull and van Seville, 2016; Furue, 2019; Middleton and Cirano, 2002; Richardson et al., 2019; Stellema et al., 2019; Wijeratne et al., 2018; Woo and Pattiaratchi, 2008) and enters the Indian Ocean south of Australia. Around the region of Cape Leeuwin, the Flinders Current splits into one westward and another northward-flowing branch (Fig. 1). While the westward flowing branch flows into the Southern Indian Ocean Gyre along the Broken Ridge, the northward-flowing branch merges with the LUC in the area of Cape Leeuwin (Koch-Larrouy et al., 2010; Middleton and Cirano, 2002; Richardson et al., 2019; Schloesser, 2014; Wijeratne et al., 2018; Woo and Pattiaratchi, 2008). This distinct northward-flowing undercurrent exists below the LC between 250 and 500 m depth and transports cool oxygen-rich waters north along the West Australian shelf (Domingues et al., 2007; Richardson et al., 2019; Schloesser, 2014; Wijeratne et al., 2018; Woo and Pattiaratchi, 2008). Today the LUC thus carries cool, nutrient-rich, and oxygenated SAMW northward

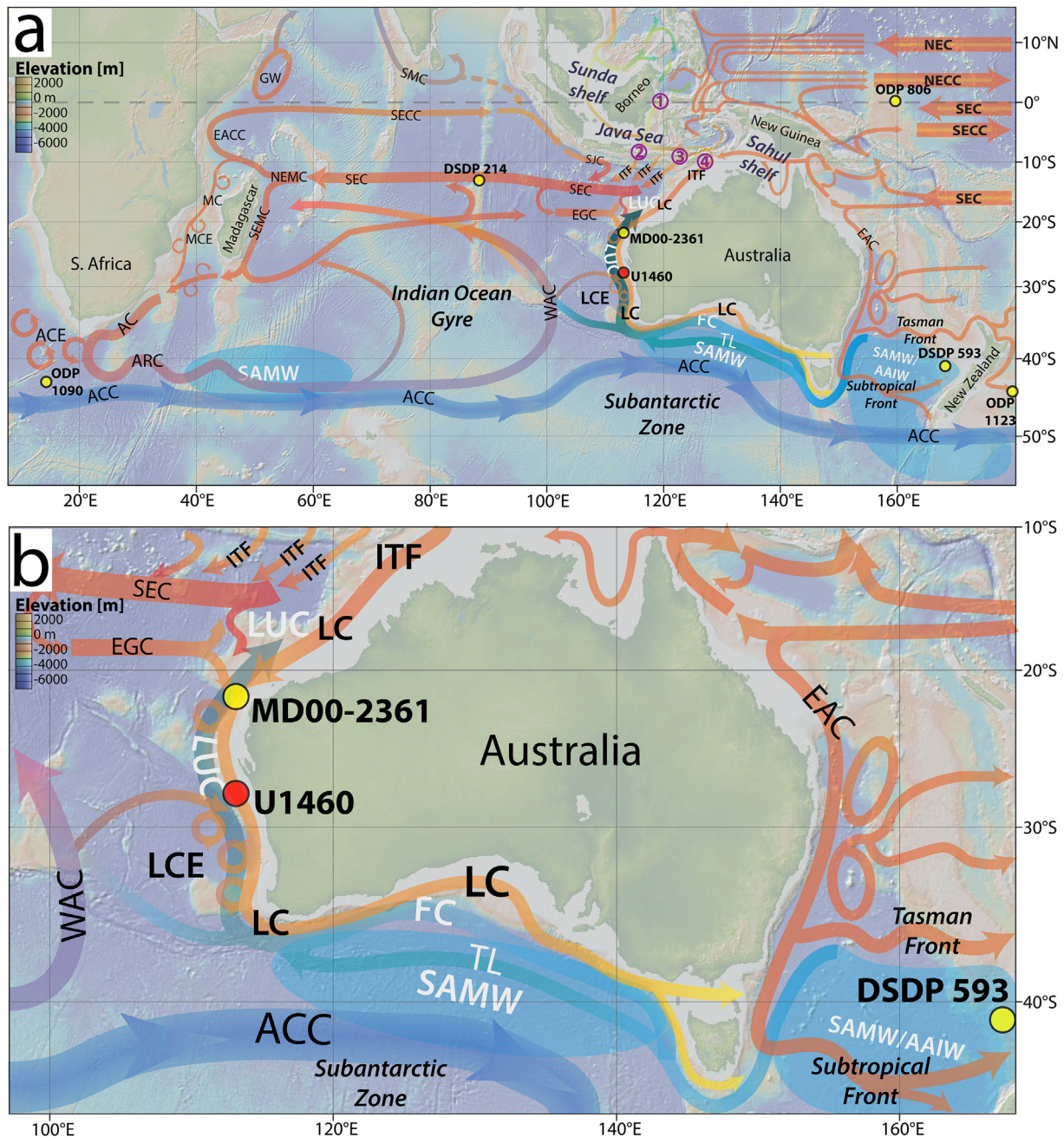


**Fig. 1.** a) General circulation map of the southern Indian Ocean during northern hemisphere summer (oceanographic data adapted from Koch-Larrouy et al., 2010; Richardson et al., 2019; Schott et al., 2009; You, 1998). b) Closeup of the current conditions around Australia. Site U1460 (red) and additional Sites referred to in this study (yellow). The base map was generated with GeoMapApp (Ryan et al., 2009). Note the connection of the Leeuwin Current (LC) and its eddies (LCE) via the Sahul shelf to the outflow of the Indonesian Throughflow (ITF). Below the LC, the northward-flowing Leeuwin Undercurrent (LUC) is sourced south of Australia from the Flinders Current (FC) and the Tasman Leakage (TL). Areas of sub-Antarctic mode water (SAMW) subduction are shaded in blue. Other currents shown: The Indian and Pacific Ocean South Equatorial Current (SEC), South Equatorial Counter Current (SECC), and the Pacific North Equatorial Current (NEC) and North Equatorial Counter Current (NECC), the Northeast and Southeast Madagascar Current (NEMC and SEMC), the East Australian Current (EAC), East African Coastal Current (EACC), South Java Current (SJC), Mozambique Current (MC), Mozambique Current Eddies (MCE), Agulhas Return Current (ARC), Antarctic Circumpolar Current (ACC), West Australia Current (WA). ITF paths: 1) Makassar Strait; 2) Lombok Strait; 3) Ombai Strait; 4) Timor Passage.

underneath the warm tropical and oligotrophic LC (Richardson et al., 2019; Wijeratne et al., 2018; Woo and Pattiaratchi, 2008), which significantly affects bottom water communities along the western shelf of Australia (Fromont et al., 2012; Williams et al., 2010).

Underneath the southern Indian Ocean Gyre, the South Australian SAMW mixes with other Indian Ocean SAMW that is predominantly formed and ventilated south of 30°S in the

southwestern Indian Ocean (west of 72°E) (Koch-Larrouy et al., 2010; You, 1998) and migrates northward along a distinct density surface between 1000 and 1800 m water depth (Fine, 1993; Koch-Larrouy et al., 2010).

Through air-sea interactions along the Antarctic circumpolar current (ACC), some of this SAMW is, however, also slowly transformed into Antarctic Intermediate Water (AAIW) that subducts in the Pacific sector. Thus, AAIW represents the coldest and densest

endmember of SAMW in the oceans (Sloyan and Rintoul, 2001; Koch-Larrouy et al., 2010). As mentioned above, a portion of AAIW flows back into the Indian Ocean south of Australia via the TL, thereby closing the southern loop of the global gyre circulation (Fine, 1993; Koch-Larrouy et al., 2010; Richardson et al., 2019; Ridgway and Dunn, 2007; Rosell-Fieschi et al., 2013; van Sebille et al., 2014).

### 3. Materials and methods

International Ocean Discovery Project (IODP) Site U1460 (214.5 mbsl, 27°22.5'S, 112° 55.43'E) was drilled during IODP Expedition 356 in the northern Perth Basin and yielded an expanded Pliocene record of outer neritic to shallow bathyal ramp carbonates from the Carnarvon ramp (Gallagher et al., 2017, Fig. 1). Site U1460 lies about 33 km from the Houtman Abrolhos reef, the southernmost tropical reefs in the Indian Ocean (Fig. 1; Gallagher et al., 2017).

A total of 248 samples were taken from the core material of Hole U1460A between 61.7 and 161.95 m CSF-A (corresponding to an interval between section 356-U1460A-14F-3 and 356-U1460A-35F-4) with an average spacing of ~40 cm. Several cores also showed several-decimeter-thick layers of gravel-sized bioclastic material described as "fall-in" by the shipboard science party (Gallagher et al., 2017). We did not sample this bioclastic material to avoid sampling biases in nannofossil and geochemical data, as the fine fraction (i.e., silt to clay size) was absent in these intervals.

Site U1460 Hole A and Hole B were correlated using shipboard natural gamma radiation (NGR) results (Gallagher et al., 2017), permitting a direct comparison of records derived from both holes. Allowing us to compare x-ray fluorescence (XRF) core scanning and TEX86 records generated on samples from Hole U1460B and published in Petrick et al. (2019) with the data generated for this study (Fig. 2).

#### 3.1. Quantitative nannofossil counts

For quantitative nannofossil counts, we analyzed 171 samples following the "drop method" of Bordiga et al. (2015) and the procedures outlined in Auer et al. (2019) to generate total nannofossil abundances per gram of sediment. Slides were examined using standard polarized light microscopy (Olympus BX53, Japan Agency for Marine-Earth Science and Technology, JAMSTEC) and scanning electron microscopy imaging (Zeiss Gemini DSM 982, University of Graz). Absolute alkenone-producing nannofossils (APN) abundance estimates are given as the sum of the number of APN placoliths per gram of sediment ( $N_{APN/g}$ ). For generating APN abundances, we used all known members of the Order Isochrysidales encountered in our sample material: small *Gephyrocapsa* spp. (<3  $\mu\text{m}$ ); all *Gephyrocapsa* spp. > 3  $\mu\text{m}$  (including the taxa *G. oceanica*/*G. omega*, *G. caribbeanica*), *Pseudoemiliania lacunosa* (including *P. ovata*), and all *Reticulofenestra* spp. (including *R. asanoi*). Absolute nannofossil and APN abundance estimates were converted to total nannofossil and alkenone producing nannofossil accumulation rates (NAR and APN-ARs respectively; Figs. 3c and 4a) following the methodology outlined in section 3.2.1. For the current study, we focus solely on total Nannofossil and APN accumulation rates to better understand total coccolith accumulation in comparison to organic carbon flux at Site U1460 over the MPT. Full assemblage data will be presented elsewhere.

##### 3.1.1. Taxonomic notes

Nannofossil taxonomy in this study follows the framework outlined in Perch-Nielsen (1985) and Young (1998), as well as the Nannotax3 website (Young et al., 2014) and follows the general size

definition of *Gephyrocapsa* spp. outlined in Raffi et al. (2006). However, due to the high abundance of small *Gephyrocapsa* placoliths <3  $\mu\text{m}$  (Fig. 2a), we further grouped these specimens as small *Gephyrocapsa* spp. following the size ranges outlined in Young et al. (1997). The taxonomic concept of Sato and Takayama (1992) was used to determine abundances of the taxon *Reticulofenestra asanoi*.

### 3.2. Geochemistry and geophysics

#### 3.2.1. Organic carbon and calcite equivalent carbonate content

For TOC and weight content determination (Fig. 4c), ~0.1 g of freeze-dried and ground sample was fully decalcified using step-wise addition of 2 N HCl. After decalcification, samples were washed with distilled water to remove excess HCl and dried and measured using a LECO CS300 carbon and sulfur analyzer at the University of Graz. Total carbon (TC) weight content was also determined separately by analyzing ~0.1 g of bulk sediment. All measurements were performed in triplicate to evaluate analytical precision as well as sample inhomogeneities.

To calculate calcite equivalent carbonate ( $\text{CaCO}_3(\text{eq.})$ ) weight content, we used the stoichiometric formula  $\text{CaCO}_3(\text{eq.}) = (\text{TC} - \text{TOC}) \times 8.333$  (Stax and Stein, 1995, Fig. 3a). Mass accumulation rates (MARs) of organic carbon (Fig. 4e) were calculated by multiplying the TOC content with bulk MARs. Bulk MARs were calculated using the formula:

$$\text{BMAR} = \text{LSR} \times \text{DBD}$$

where BMAR is the bulk mass accumulation rate, LSR is the linear sedimentation rate [cm/kyr] (Fig. 4b), and DBD is the dry bulk density [ $\text{g}/\text{cm}^3$ ] derived from neutron porosity logs and shipboard moisture and density data (Gallagher et al., 2017).

#### 3.2.2. NGR derived uranium concentrations and their relation to organic carbon fluxes

During Expedition 356, natural gamma radiation (NGR) spectra of the recovered sediments were measured using the whole-round section logger (Gallagher et al., 2017). These spectra can be used to quantify the sedimentary uranium content through a freely available algorithm published by De Vleeschouwer et al. (2017). Uranium content was converted into uranium accumulation rates (Fig. 4f) in the same way as organic carbon accumulation rates.

Uranium is a soluble trace element transported easily and precipitated far from its source in association with carbonates and organic materials. In carbonate rocks, U is often the dominant gamma-ray source (Doveton, 1991; Raddadi et al., 2005). Dissolved U concentrations in the water column are relatively unresponsive to changes caused by varying terrigenous input since U is known to have a long residence time in the ocean (200–400 kyr) (Anderson, 1982; Ku et al., 1977; McManus et al., 2005; Veeh et al., 1974).

Several studies show a strong relationship between U precipitation, organic carbon rain, and prevailing redox conditions (McManus et al., 2005; Yamada et al., 2006). Authigenic U uptake by the sediment is also mostly independent of possible subsequent oxidation and dissolution of organic matter (McManus et al., 2005), making U an accurate relative proxy for the total organic carbon flux to the ocean floor (Anderson et al., 2002; Auer et al., 2016; Chase et al., 2001; McManus et al., 2005). Uranium accumulation is thus a proxy for net-primary productivity (McCorkle et al., 1994; McManus et al., 2005). Uranium bound in a stable mineral phase is also very stable during subsequent diagenetic processes (Auer et al., 2016; McManus et al., 2005). We thus assume that direct enrichment of U through organic matter fluxes to the seafloor and subsequent authigenic mineralization was the most likely source for the observed variations in local U concentrations. Uranium

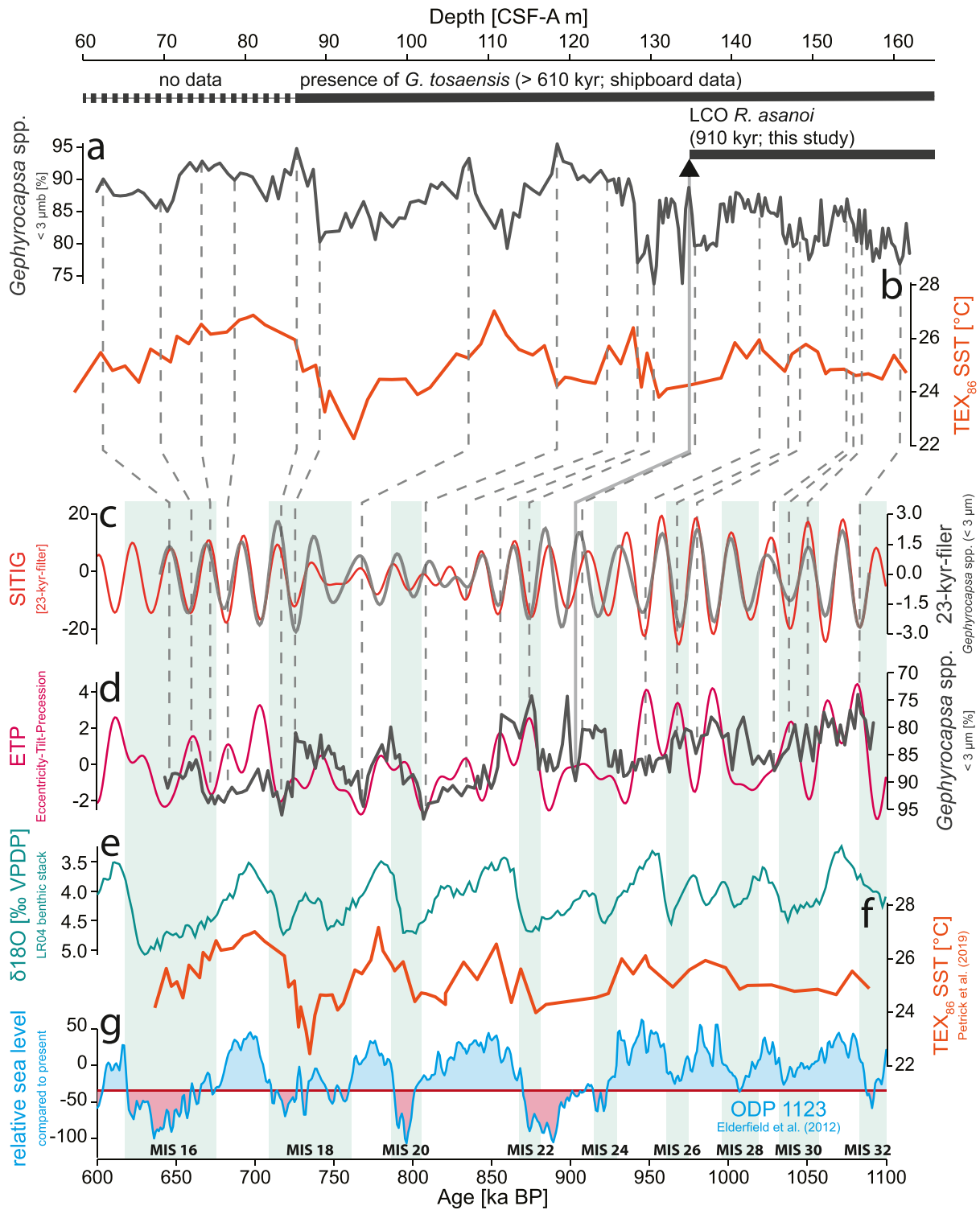


**Fig. 2.** Site U1460 age-depth model. The LCO of *R. asanoi* is used as the primary biostratigraphic tie point, with additional age information provided by the shipboard record of *G. tosaensis*. **a)** Relative abundance of *Gephyrocapsa* spp. (<3 μm) (Hole U1460A; this study) in depth (CSF-A) with associated tie points; **b)** TEX<sub>86</sub> SSTs generated for U1460B (Petrick et al., 2019) in depth (CSF-A); **c)** Summer (21 June) inter-tropical insolation gradient (SITIG; Bosmans et al., 2015) 23-kyr-filter tuning target compared to the *Gephyrocapsa* spp. (<3 μm) 23-kyr-filter using the presented tie lines; **d)** comparison of inverted *Gephyrocapsa* spp. (<3 μm) relative abundance variation with austral ETP; **e)** inverted LR04 benthic δ<sup>18</sup>O stack of Lisiecki and Raymo (2005) compared to **f)** the retuned SST record from U1460B transferred to the age model generated for this study; **g)** Sea level curve of Elderfield et al. (2012). Large (>45 m below present) lowstands are marked by the red shaded areas.

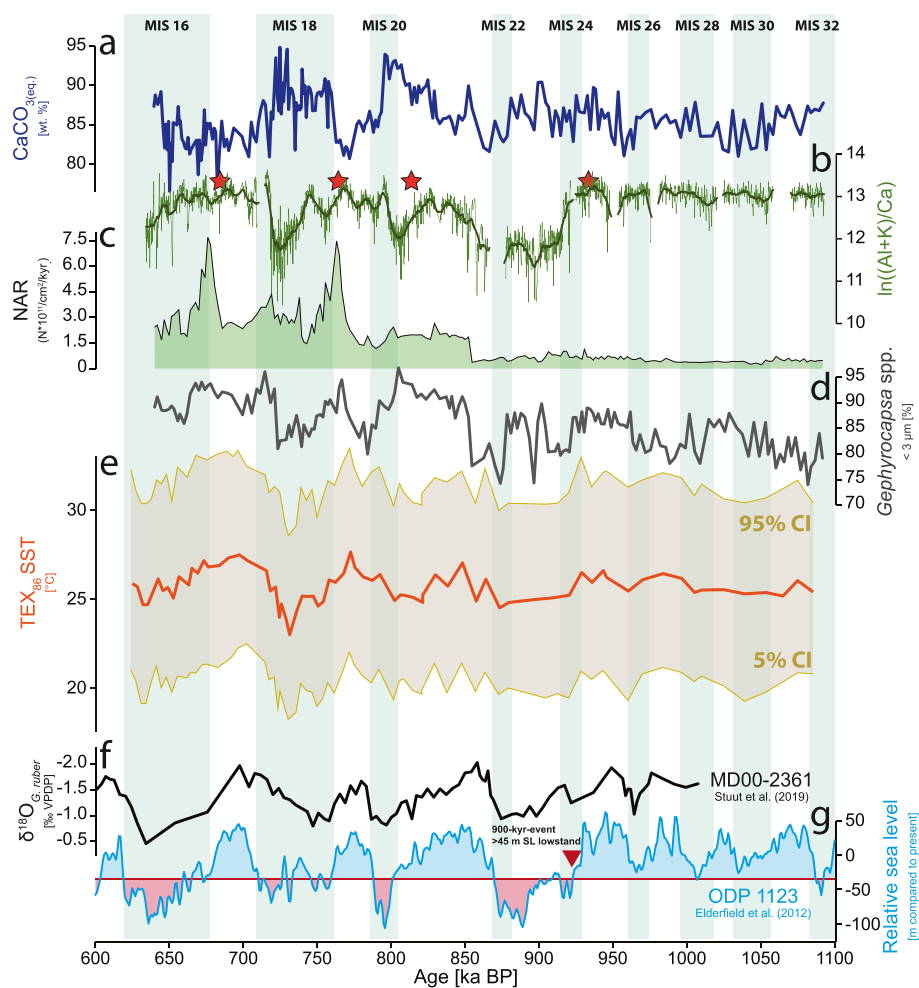


**Fig. 3.** Local carbonate content together with terrigenous and pelagic fluxes (based on total nanofossil accumulation rates) at Site U1460 compared to SST,  $\delta^{18}\text{O}$ , and sea level records. **a)** Calcite equivalent carbonate content ( $\text{CaCO}_3(\text{eq.})$ ); **b)**  $\ln((\text{Al} + \text{K})/\text{Ca})$  elemental ratio as XRF derived terrigenous influx proxy; **c)** pelagic carbonate production based on total nanofossil accumulation rate (NAR); **d)** relative abundance of small *Gephyrocapsa* spp. ( $<3 \mu\text{m}$ ) showing a contemporaneous abundance increase with NAR  $\sim 850$  ka; **e)**  $\text{TEX}^{86}$  SSTs for Site U1460 with its BAYSPAR (Tierney and Tingley, 2014) derived 95% and 5% confidence intervals (data derived from Petrick et al., 2019); **f)** *Globigerinoides ruber* derived  $\delta^{18}\text{O}$  record from adjacent Site MD00-2361 (see Fig. 1; Stuut et al., 2019); **g)** Relative sea level reconstruction (compared to current sea level) of Elderfield et al. (2012) from ODP Site 1123, note the inception of large ( $>45$  m below present) sea level drops during MIS 24 (marked as red arrow and red shaded areas).

incorporated into a stable mineral phase thus provides an additional proxy of organic matter flux in high-carbonate low-terrigenous influx sediments independent of organic matter remineralization and consumption by benthic organisms (e.g., Auer et al., 2016).

This U proxy interpretation, although well established, was scrutinized by comparing U evolution with other proxy data for the U1460 MPT interval (Fig. 4). Our data clearly shows a co-evolution of measured TOC (wt. %), and NGR derived U ( $\mu\text{g/g}$ ) concentrations on G-IG times. This pattern remains stable even when comparing calculated MARS of the two proxies. To determine if these proxies for overall TOC accumulation correlate with surface water productivity and surface-to-bottom organic carbon fluxes, we utilize the  $\text{C}_{37}$  Alkenone MARS (Fig. 4g). Alkenone and U MARS rates also co-vary on G-IG scales, which further supports the assumption that the high-resolution NGR derived U content are reflective of surface water productivity derived organic matter fluxes at Site U1460 (Fig. 4c–g) in accordance with previous findings from the Perth Basin (McCorkle et al., 1994; Veeh et al., 2000).

### 3.3. Alkenones

Alkenone and glycerol dialkyl glycerol tetraethers (GDGT)

analyses were carried out at the Max Planck Institute of Chemistry in Mainz, Germany. For analyses, the samples were freeze-dried, gently disaggregated, and extracted using an ASE350 extraction system using the methods described in Auderset et al. (2020). Briefly, polar (GDGT) and non-polar (alkenone) fractions were separated using simultaneous extraction and silica separation within the ASE cells and subsequently dried using a Thermo Rocket evaporator. Alkenone concentration was determined via an Agilent 7890 B gas chromatography (GC) system using hexatriacontane and 2-nonadecanone as internal standards. The polar GDGT fraction was analyzed in an Agilent HPLC-MS system as reported in Petrick et al. (2019). Sea surface temperatures were calculated using the BAYSPAR method of Tierney and Tingley (2014).

### 3.4. Spectral analysis

For spectral analyses, we used REDFIT spectra (Schulz and Mudelsee, 2002) and Wavelet spectra as implemented in the statistic package PAST (v. 4.03) (Hammer et al., 2001). Significant peaks were selected based on Monte Carlo corrected confidence intervals (CI) and their clarity in the resulting power spectra (Fig. 5 and Fig. S1 in the supplementary materials; Table 1). Gaussian bandpass filtering was performed in the R package 'astrochron'

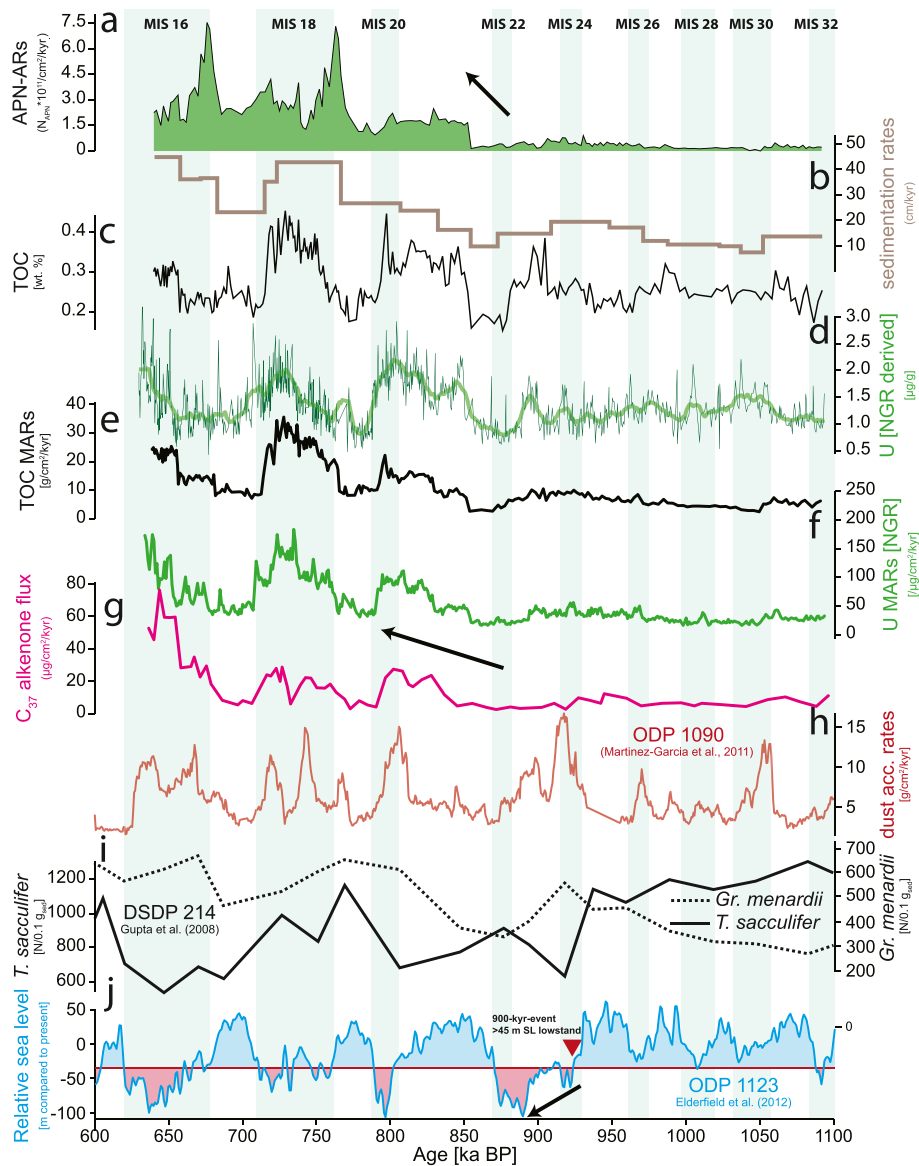


**Fig. 4.** Comparison of organic matter flux and productivity data at Site U1460 with equatorial Indian ocean surface water conditions (Gupta et al., 2008), Southern Ocean dust flux (Martinez-Garcia et al., 2011), and sea level data (Elderfield et al., 2012). **a)** Alkenone producing nannofossil accumulation rates (APN-ARs) ( $N \times 10^{11}/\text{cm}^2/\text{kyr}$ ) note the low correlation with  $C_{37}$  alkenone MARS; **b)** Sediment accumulation rates ( $\text{cm}/\text{kyr}$ ); **c)** Bulk total organic carbon (TOC) in wt. % for Site U1460; **d)** Shipboard natural gamma radiation (Gallagher et al., 2017) derived U content in p.p.m. ( $= \mu\text{g}/\text{g}$ ); **e)** Total organic carbon MARS ( $\text{g}/\text{cm}^2/\text{kyr}$ ) for Site U1460; **f)** Uranium MARS for Site U1460 ( $\mu\text{g}/\text{cm}^2/\text{kyr}$ ); **g)**  $C_{37}$  Alkenone MARS at Site U1460 derived from data published in Petrick et al. (2019) note the co-variation with U and TOC MARS; **h)** Southern Ocean dust flux ( $\text{g}/\text{cm}^2/\text{kyr}$ ) from Martinez-Garcia et al. (2011); **i)** absolute abundance shifts in the accumulation of *T. sacculifer* versus *Gr. menardii* at equatorial Indian ocean DSDP Site 214 from Gupta et al. (2008); note the abundance drop in *T. sacculifer* within MIS 24 as well as continuously rising *Gr. menardii* abundances; **j)** Sea level reconstruction of Elderfield et al. (2012) from ODP Site 1123 as a reference for global G-IG changes, note the inception of large ( $>45$  m below present) sea level drops during MIS-24 (marked as a red arrow).

(Meyers, 2014) using a frequency window with upper and lower bounds defined as  $\pm 25\%$  of the target frequency (Figs. 2 and 6). The ETP target curve was also generated using the R package 'astrochron' (Meyers, 2014), applying equal weights to eccentricity, obliquity, and precession. Precession was set to positively contribute to ETP when the perihelion was reached during the SH summer half-year. The applied tuning approach followed the best practice guidelines of Sinnesael et al. (2019).

### 3.5. X-ray fluorescence analyses

The X-ray fluorescence (XRF)-core scanning data was obtained using a third-generation Avaatech XRF core scanner at the XRF Core

Scanning Facility of the Gulf Coast Repository at Texas A&M University. X-ray spectra were acquired using a Canberra X-PIPS Silicon Drift Detector (SDD; Model SXD 15C-150-500) with 150 eV X-ray resolution, the Canberra Digital Spectrum Analyzer DAS 1000, and an Oxford Instruments 50 W XTF5011 X-Ray tube with rhodium (Rh) target material. Measurements were performed on a 2 cm resolution and processed using the iterative least square software (WIN AXIL) package from Canberra Eurisys (see Petrick et al., 2019). XRF data is reported as the natural logarithm of multi-element composite ratios (Table S2). We applied the  $\ln((\text{Al} + \text{K})/\text{Ca})$  ratio as a proxy for terrigenous influx (see Auer et al., 2019) and compared this record to bulk carbonate content (Fig. 3a and b). Moreover, we adopted the  $\ln(\text{Si}/(\text{Al} + \text{Ca}))$  ratio as a proxy

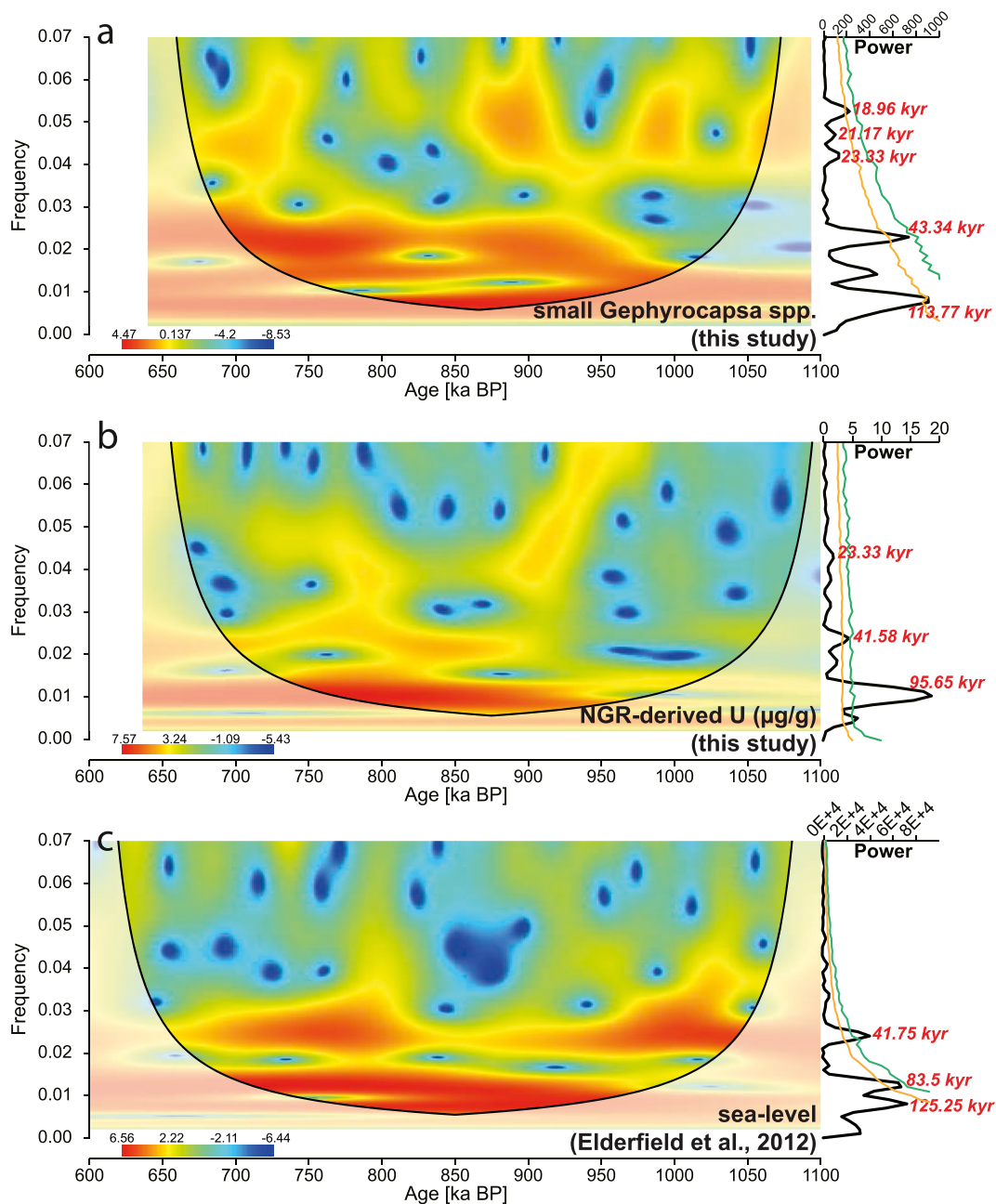


**Fig. 5.** Wavelet analysis and REDFIT spectra showing the significant periodicities in kyr (see Table 1) of **a)** *Gephyrocapsa* spp. (<3  $\mu\text{m}$ ); **b)** Natural gamma radiation (NGR) derived U content in p.p.m. (=  $\mu\text{g/g}$ ); **c)** relative sea level record of ODP Site 1123 (Elderfield et al., 2012). REDFIT spectra show the 99% (green) and 95% (orange) confidence intervals according to the results presented and supplementary Fig. S1.

for biogenic silica (Fig. 7a). We normalized the XRF Si counts to the sum of Ca and Al to account for both biogenic carbonates, as well as the potential (but likely very minor) contribution of terrigenous influx derived silicates at Site U1460. The resulting biogenic silica estimates were then compared to the siliceous sponge spicule abundances generated during Expedition 356 on a one per half-core ( $\sim 4.5$  m) resolution (Gallagher et al., 2017, Fig. 7a) as a qualitative test of the proxy.

## 4. Results

### 4.1. Biostratigraphy and orbital tuning

We defined the study's target interval between 61.72 and

161.93 m CSF-A based on the shipboard age model of Site U1460 (Gallagher et al., 2017). The shipboard biostratigraphic datums were subsequently used by Petrick et al. (2019) to generate a tuned age model for Site U1460. The tuning of Petrick et al. (2019) relies on a direct correlation of  $\text{TEX}_{86}$  temperature and XRF  $\log(\text{Ca}/\text{Ti})$  records to the LR04 benthic  $\delta^{18}\text{O}$  stack of Lisiecki and Raymo (2005). As the initial tuning of Petrick et al. (2019), however, only relied on the initial shipboard age model, it did not have the necessary resolution for the present study. Using new higher resolution nannofossil biostratigraphic data with an average 2.6 kyr sample spacing, we further refined their tuning by narrowing the uncertainty of the last common occurrence (LCO) of *Reticulofenestra asanoi*, providing better constraints for the MPT at Site U1460 (Fig. 2).

**Table 1**

Significant frequency (1/kyr) of the REDFIT analysis (Fig. S1 in the supplementary file) of the relative abundance of *Gephyrocapsa* spp. (<3  $\mu\text{m}$ ), natural gamma radiation derived U content ( $\mu\text{g/g}$ ), and sea level (Elderfield et al., 2012) are given with their Monte Carlo corrected AR1 confidence level, as well as their periodicity (in kyr) and the corresponding orbital parameters derived from the LA04 solution (Laskar et al., 2004); note that "eccentricity" is likely dominated by the quasi-100-kyr G-IG cycles.

|  | Frequency (1/kyr) | Confidence (% MoCa AR1) | Periodicity (kyr) | Orbital parameter (Laskar et al., 2004) |
|--|-------------------|-------------------------|-------------------|---|
| <i>Gephyrocapsa</i> spp. (<3 $\mu\text{m}$ ) (this study)    | 0.0087894         | >95%                    | 113.8             | Eccentricity                            |
|  | 0.023072          | >95%                    | 43.3              | Obliquity                               |
|  | 0.040651          | <80%                    | 23.3              | Precession                              |
|  | 0.047243          | <80%                    | 21.2              | Precession                              |
|  | 0.052737          | >95%                    | 19.0              | Precession                              |
|  | 0.095585          | >99%                    | 10.5              | Half Precession?                        |
| U ( $\mu\text{g/g}$ ) (this study)                           | 0.010455          | >99%                    | 95.6              | Eccentricity                            |
|  | 0.024047          | >95%                    | 41.6              | Obliquity                               |
|  | 0.042866          | >80%                    | 23.3              | Precession                              |
|  | 0.007984          | >90%                    | 125.3             | Eccentricity                            |
| sea level (re-analysis of data from Elderfield et al., 2012) | 0.011976          | >95%                    | 83.5              | Eccentricity                            |
|  | 0.023952          | >99%                    | 41.8              | Obliquity                               |

The abundance of *R. asanoi* was very low (<4%) compared to available open ocean records (Lupi et al., 2012; Marino et al., 2009). Our counts show that *Reticulofenestra* sp. specimen (diameter of 6–6.4  $\mu\text{m}$ ) occur throughout the studied interval (Table S1 in the supplementary data). These specimens were difficult to distinguish unequivocally from *R. asanoi* due to poorer nanofossil preservation in the upper parts of the study interval. Nevertheless, the LCO of *R. asanoi* was defined at a depth between 135.12 and 135.42 m CSF-A, based on the last occurrence of unequivocal *R. asanoi* specimens following the definition of Sato and Takayama (1992). We can thus correlate this depth to the globally synchronous LCO of *R. asanoi* ~910 ka BP (Backman et al., 2012; Raffi et al., 2006 and references therein).

This updated LCO of *R. asanoi* was incorporated as the primary biostratigraphic tie point into our subsequent tuning. We further supplemented biostratigraphic information by the sparse ship-board biostratigraphic information that indicates the presence of *Globorotalia tosaensis* in Core 19 F-CC at a depth of 86.59 m CSF-A (Fig. 2). Although no planktonic foraminifer data is available between cores 19 F-CC and 2 F-CC (Gallagher et al., 2017), the presence of *G. tosaensis* indicates that material from Section 356-U1460A-19 F-CC is older than 0.61 Ma (Wade et al., 2011).

Initial tuning then follows the approach of Petrick et al. (2019) correlating TEX<sub>86</sub> temperature maxima with  $\delta^{18}\text{O}$  minima in the LR04 benthic  $\delta^{18}\text{O}$  stack of Lisiecki and Raymo (2005). The tuning based on our new biostratigraphic information resulted in a revision of the original age–depth model of Petrick et al. (2019) within our study interval. Following this correlation of the record on a G-IG scale, we further refined the tuning using an orbital tuning approach based on the correlation of the abundance variations in percent of small (<3  $\mu\text{m}$ ) *Gephyrocapsa* spp. to a summer (21 June) inter-tropical insolation gradient (SITIG; see Bosmans et al., 2015) target. We assumed a positive phase relationship, as maximum high inter-tropical insolation gradients enhance the pressure gradients favorable for stronger LC intensity (De Vleeschouwer et al., 2019). The SITIG was chosen as a tuning target because its variation was found to reflect changes in LC dynamics (see De Vleeschouwer et al., 2019), and the abundance of the opportunistic bloom-forming small *Gephyrocapsa* spp. was likely controlled by changes in LC strength (Takahashi and Okada, 2000). By choosing a parsimonious tuning approach, we achieved a good fit with SITIG (Bosmans et al., 2015, Fig. 2c), using only 19 tie points routed in both significant maxima and minima in our small *Gephyrocapsa* spp. record. These 19 tie points are provided in the supplementary data.

The fit of the tuning is shown using the 23 kyr bandpass filter of *Gephyrocapsa* spp. overlain on the 23-kyr-filter of the SITIG. This

tuning approach further resulted in an inverse correlation of the relative abundances of small *Gephyrocapsa* spp. with the eccentricity-tilt-precession (ETP) composite and the amplitude variability of the austral summer insolation at 28°S (Figs. 2c and 6a). The results of our independent tuning place the LCO of *R. asanoi* between c. 905–907 ka BP in Hole U1460A, which fits with the established LCO of the taxon around 900–910 ka BP (Fig. 2d; Raffi et al., 2006). Finally, we updated XRF and TEX86 data of Petrick et al. (2019) to our new age model to compare them directly in the time domain (Fig. 2f).

#### 4.2. Calcareous nanofossil accumulation

Nanofossil preservation is generally moderate to good although early diagenetic overgrowth was detected frequently. Total nanofossil abundance estimates vary between  $0.14 \cdot 10^{10}$  and  $1.24 \cdot 10^{10}$  N<sub>NAR</sub>/g (Fig. 3c), with total alkenone producing nanofossils ranging between  $0.13 \cdot 10^{10}$  and  $1.20 \cdot 10^{10}$  N<sub>APN-AR</sub>/g (Fig. 4a). Placoliths of alkenone producing taxa represent on average 96.33% (min. = 91.91%; max. = 98.81%) of the whole assemblage and are dominated by small *Gephyrocapsa* spp. Total NAR show a marked increase between 128.39 and 127.59 m CSF-A (~850 ka), doubling in abundance from  $\sim 0.20 \cdot 10^{10}$  to  $0.51 \cdot 10^{10}$  N/g, which is also reflected in APN-MARs (Fig. 4a). This marked increase in nanofossil abundance is also accompanied by an increase in the relative abundance of small *Gephyrocapsa* spp. (Fig. 2a). Similarly, we observed no direct linear correlation (interpolated to 1 kyr sample spacing;  $n = 453$ ) between NAR and  $\text{CaCO}_3(\text{eq.})$  ( $r = -0.12$ ; Fig. 3). During the MIS 21 sea level highstand, this relationship changes and becomes more striking. Considering only the interval between 850 and 640 ka BP we found a negative correlation ( $r = -0.43$ ) between  $\text{CaCO}_3(\text{eq.})$  and nanofossil accumulation rates. It is also noteworthy that the highest TOC/U and alkenone MARs show a different pattern to APN-ARs after MIS 22 (Fig. 4a), where peaks in these productivity records show no corresponding peaks in APN-ARs.

#### 4.3. XRF terrigenous influx and carbonate content

X-ray fluorescence analyses reveal an inverse correlation between the  $\ln((\text{Al} + \text{K})/\text{Ca})$  ratio with  $\text{CaCO}_3(\text{eq.})$  (Fig. 3) starting with MIS 21 ( $r = -0.55$ ; based on linearly interpolated 1 kyr sample spacing;  $N = 453$ ). The interval between 1100 and ~900 ka shows stable and comparatively high terrigenous influx (Fig. 3b), which shows no correlation with the recorded carbonate content variability ( $r = -0.06$ ). Following the sea level drop during the 900-ka event (MIS 24–22), the  $\ln((\text{Al} + \text{K})/\text{Ca})$  ratio decreases, while carbonate content only increases to a minor degree. The following

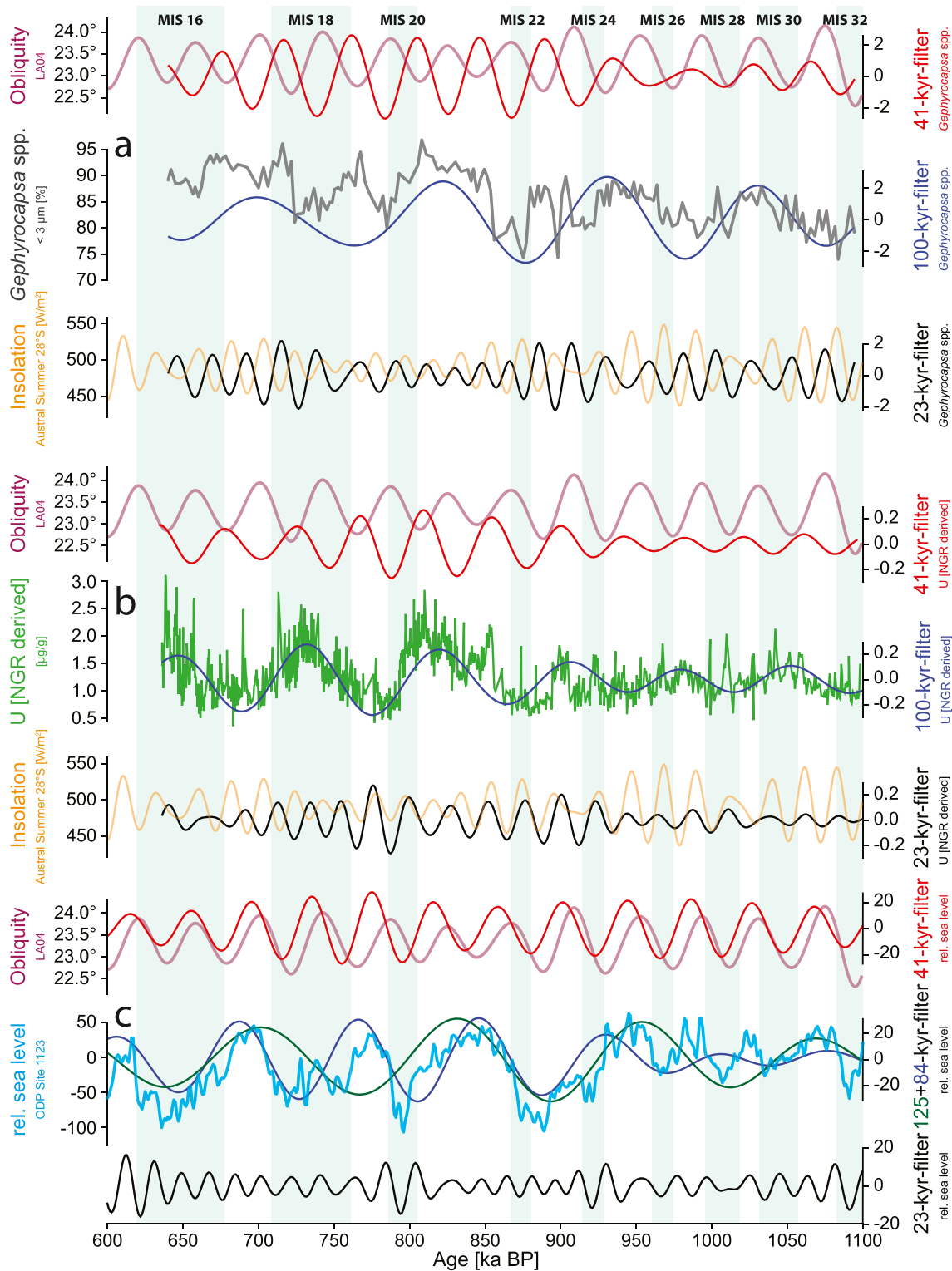


**Fig. 6.** Gaussian bandpass filters corresponding to the quasi-100-kyr/eccentricity cycles, the 41-kyr orbital obliquity cycle, as well as the ~23-kyr precessional insolation cycle of **a)** the relative abundance of *Gephyrocapsa* spp. (<math>< 3 \mu\text{m}</math>); **b)** Natural gamma-radiation (NGR) derived U content; **c)** The relative sea level reconstructions at ODP Site 1123 (Elderfield et al., 2012) in comparison to austral summer insolation at 28°S and orbital obliquity (Laskar et al., 2004).

interglacial (MIS 21e-g; Railsback et al., 2015) shows an initial reduction in carbonate content, as well as the initiation of a clear G-IG pattern in the  $\ln((Al + K)/Ca)$  ratio. This G-IG pattern is closely mirrored by carbonate content, with the highest terrigenous influx and lowest carbonate content generally detected during

interglacials (i.e., MIS 21e-g, 19c and 17c). We note that terrigenous flux minima and highest carbonate content are generally associated with sea level falls in the sea level reconstruction of Elderfield et al. (2012; Fig. 3g) after MIS 22, with values rising again at the apex of the subsequent glacial sea level lowstands.

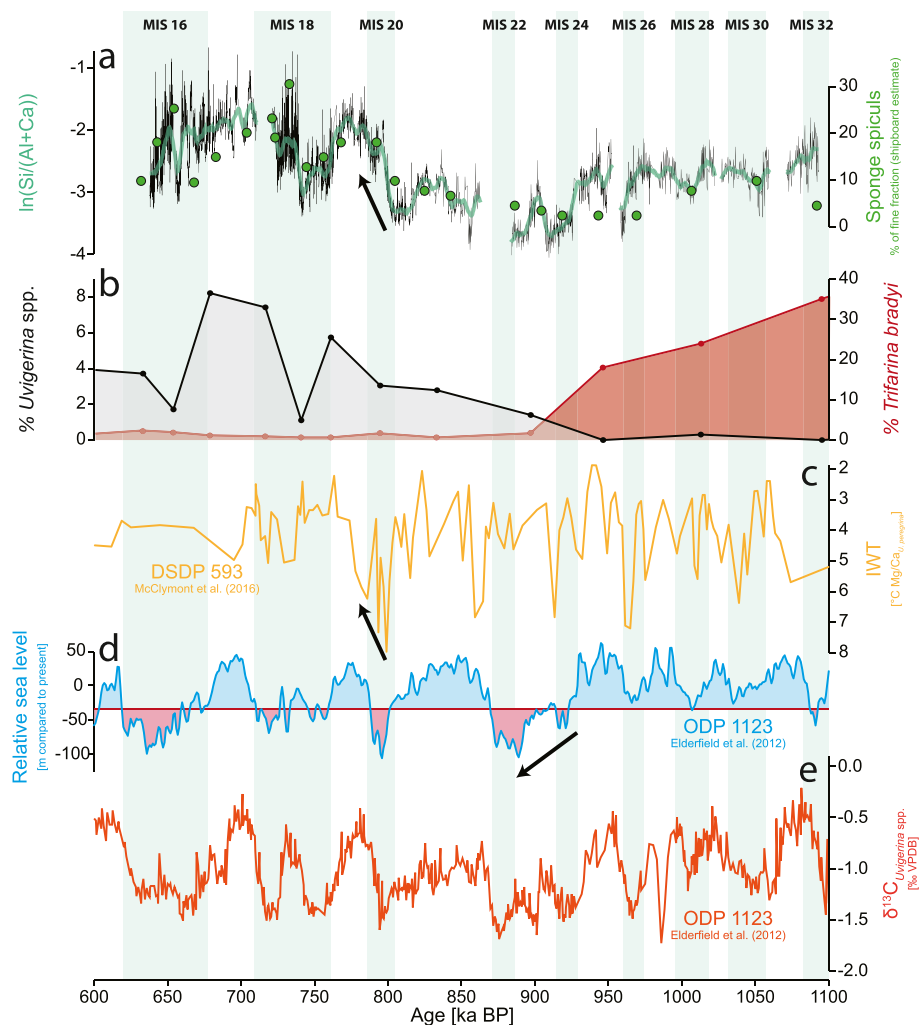


**Fig. 7.** Leeuwin Undercurrent proxies in comparison to global data. **a)** XRF-core scanning derived sponge spicule record (for U1460B) based on the  $\ln(\text{Si}/(\text{Al} + \text{Ca}))$  elemental ratio compared to the shipboard abundance estimates of siliceous spicule in the fine fraction (data from Hole U1460A; Gallagher et al., 2017). Note the close correlation between data from Hole A and B; **b)** abundance of detritive *Uvigerina* spp. and facultative anaerobe *Trifarina bradyi* from U1460 benthic foraminifera abundance data of Haller et al. (2018), with a clear cross-over in the two abundance during the 900-ka event (Mis 24–22); **c)** inverted *Uvigerina peregrina* Mg/Ca ratio derived intermediate water temperatures (IWT, in °C) from DSDP Site 593 (see Fig. 1). Note the IWT drop and concomitant spicule increase in MIS 20–19; **d)** global sea level from ODP Site 1123 (Elderfield et al., 2012), note the inception of large (>45 m below present marked by the red shaded areas) sea level drops during MIS- 24; **e)** Lower central deep-water *U. peregrina* derived  $\delta^{13}\text{C}$  records from ODP Site 1123 (Elderfield et al., 2012). Note the co-variation of spicule abundances and deep water  $\delta^{13}\text{C}$  on G-IG scales starting with MIS 20.

#### 4.4. Organic matter, uranium, and alkenone content

Between ~1100 and ~920 ka, organic matter content and MARs are overall stable, with TOC ranging between ~0.2 and 0.3 wt%. During MIS 23, TOC rises significantly to ~0.4 wt% before reducing to <0.2 wt% at the end of MIS 22. During MIS 21, TOC increases again until MIS 20 (850–800 ka). After MIS 20, TOC wt.% and flux rates (in  $\text{g}/\text{cm}^2/\text{kyr}$ ) are strongly associated with the 100 kyr G-IG variability until the end of the study interval ~640 ky within MIS 16 (Fig. 4c). The described pattern in TOC wt.% and MARs co-vary with U content, especially after MIS 22 (Fig. 4d–f). Similar large-scale trends are also observed in the  $\text{C}_{37}$  alkenone MARs at Site U1460 (Fig. 4g). Linearly interpolated (1 kyr sample spacing;  $n = 453$ ) U and TOC show a positive linear correlation throughout the section ( $r = 0.52$ ). We further note a linear correlation ( $r = 0.56$ ) between TOC and  $\text{CaCO}_3(\text{eq.})$ .

#### 4.5. Spectral analyses

##### 4.5.1. Small *Gephyrocapsa* spp. abundances

The spectral analysis of the relative abundance counts of small

*Gephyrocapsa* spp. (<3  $\mu\text{m}$ ) shows significant frequency peaks (>99% CI) corresponding to ~113.8 kyr and 41 kyr, respectively (Fig. 5a, Table 1). Additionally, the abundance of small *Gephyrocapsa* spp. fully resolves precession cyclicities ~23.6 kyr and ~19.1 kyr (Laskar et al., 2004) – this, however, is to be expected as the record was tuned to the SITIG (see Fig. 2c). The respective bandpass filters of small *Gephyrocapsa* spp. and SITIG also show a close co-evolution over the tuned interval. Spectral analyses and bandpass filtering also reveal an imprint of the orbital eccentricity and obliquity component on small *Gephyrocapsa* spp. abundances. The 41-kyr-obliquity component increases in amplitude with MIS 22, while the 100 kyr eccentricity component remains stable over the studied interval. We also note that the ~23 kyr filter of small *Gephyrocapsa* spp. is out of phase with austral summer insolation at 28°S, indicating highest abundances of this taxon during southern hemisphere summer insolation minima. Finally, we detect a significant frequency peak centered ~10.5 kyr.

##### 4.5.2. NGR-derived uranium content

The REDFIT analysis of shipboard natural gamma-ray derived U content shows strong cyclicities in the eccentricity band (>95% CI

centered at ~113.8 kyr). The 41 kyr obliquity component of the REDFIT spectrum is significant (~99% CI) and well separated within the power spectrum (Fig. 5b, Table 1). REDFIT analyses detected only a minor precession component (>80% CI, centered ~23.3 kyr). Finally, we note a less significant (>80% CI) but well-separated frequency peak around ~10.3 kyr (Fig. S1 in the supplementary material). Gaussian bandpass filtering shows an increase of both the 100 kyr and the 41 kyr frequency component by MIS 22. We note that the 41 kyr frequency component is strongly anti-phased with the orbital obliquity component (Laskar et al., 2004) after MIS 24.

#### 4.5.3. Sea level (Elderfield et al., 2012)

REFFIT analyses and gaussian bandpass filtering of detected Milankovitch frequencies of the sea level curve published by Elderfield et al. (2012) were re-analyzed using the same methodologies described in section 2.4 to provide internal consistency. As revealed in the initial study (Elderfield et al., 2012), our REDFIT analysis confirms a strong imprint of the 41-kyr-obliquity cycle throughout the studied interval and two frequencies centered around 100 kyr with ~125 kyr and ~84 kyr, respectively (Fig. 5c, Table 1). Gaussian bandpass filters show an increase in the imprint of the 125 kyr and 84 kyr filter after MIS 21, while the 41-kyr-obliquity cycle is well represented throughout the study intervals and shows no significant long-term increases or decreases. We interpret these changes as indicative that both the ~84 and ~125 kyr frequencies are an expression of the quasi-periodic glacial-interglacial variability (Maslin and Brierley, 2015) during the MPT and not orbital eccentricity, or a spectral artifact of orbital obliquity.

#### 4.6. Biogenic silica accumulation

The  $\ln(\text{Si}/(\text{Ca} + \text{Al}))$  ratio shows no clear correlation with  $\text{CaCO}_{3(\text{eq.})}$  content before ~850 ky BP ( $r = -0.08$ ; linearly interpolated 1kyr sample spacing;  $n = 453$ ). After 850 ka, a strong inverse correlation is present ( $r = -0.59$ ; linearly interpolated 1 kyr sample spacing;  $n = 453$ ). Based on shipboard spicule abundance estimates (Gallagher et al., 2017), this inverse correlation is related to increased biogenic silica accumulation (i.e., from sponges) at Site U1460 during MIS 21. Shipboard spicule counts (Gallagher et al., 2017) estimated that siliceous sponge spicules compose up to 30% of the fine fraction by that time (Fig. 7a). We consequently note that carbonate content is controlled by both terrigenous influx and changing biogenic silica accumulation at Site U1460.

### 5. Discussion

#### 5.1. Terrigenous influx at site U1460

Somewhat counterintuitively, carbonate content, as well as terrigenous influx, are higher during sea level highstands than lowstands at Site U1460 (Fig. 3a and b). Terrigenous influx is further not related to planktonic carbonate accumulation changes, as shown by the patterns in NARs (Fig. 3c). The sedimentation changes between lowstand and highstand are also well supported by comparing local  $\text{TEX}_{86}$  data (Petrick et al., 2019, Fig. 3e) and Core MD00-2361 *Globigerinoides ruber*  $\delta^{18}\text{O}$  record of Stuet et al. (2019; Fig. 3f), which we used to constrain regional G-IG changes.

Considering that Site U1460 lies along the narrow Australian southwest shelf's outer edge, it becomes evident how lower sea level may lead to higher benthic carbonate production, while open marine pelagic sedimentation dominates during highstands (Deik et al., 2021; Gattuso et al., 2006). Our analysis shows that a sea level lowstand below ~45 m of present day sea level – according to the Elderfield et al. (2012) sea level reconstruction – appears to be

necessary to change the local environment towards a benthic productivity dominated setting. We suggest that the inverse relationship between sea level and carbonate accumulation is due to increased downslope transport of neritic carbonates to Site U1460 during glacial lowstands (Brandano et al., 2012; Deik et al., 2019, 2021). Winnowing within the swell wave base is also likely to have influenced carbonate sedimentation patterns (Deik et al., 2019, 2021, 2021; Gallagher et al., 2017). We note that an increase in pelagic sedimentation occurs directly with the initial rise in global sea level and coincides with increasing  $\ln((\text{Al} + \text{K})/\text{Ca})$  values. The influence of winnowing is also reflected by the presence of coarse-grained intervals of gravel-sized bioclastic material (Gallagher et al., 2017) at the beginning of sea level falls (marked as red stars in Fig. 2b) that we interpret as falling stage system tracts followed by coarser, often glauconite bearing sedimentation during glacial lowstand system tracts.

#### 5.2. Organic carbon flux on the West Australian shelf

Only sparse surface productivity records (e.g., Holbourn et al., 2005; Okada and Wells, 1997; Spooner et al., 2011; Takahashi and Okada, 2000; Kawamura et al., 2006) exist for the southeastern Indian Ocean, and as of yet, none extend beyond ~550 ka (Spooner et al., 2011). In this study, we provide a record of primary productivity fluctuations at orbital time-scales since 1100 ka. To do so, we integrate new Site U1460 productivity data from ~630 to 1100 kyr (Fig. 4) and relate them to the established terrigenous influx data in conjunction with previously-published Site U1460 SST reconstructions (Petrick et al., 2019, Fig. 3e) and planktonic oxygen isotope records from adjacent Site MD00-2361 (Stuet et al., 2019, Fig. 3f).

##### 5.2.1. Surface water productivity and organic carbon flux during the MPT

Changes in primary productivity in the equatorial eastern Indian Ocean are reflected in the Site U1460 organic carbon and organic matter flux data, which show net TOC accumulation began to change between MIS 24–22 (Fig. 4c, e). These data reflect significant oceanographic changes in the eastern Indian Ocean associated with the 900-ka event. These changes, however, do not mirror overall southern hemisphere dust flux and thus iron-fertilization-driven southern high-latitude productivity before MIS 21 (Martínez García et al., 2011, Fig. 4h). We, therefore, conclude that the productivity patterns along the West Australian shelf were not influenced by the same processes as in the sub-Antarctic Zone. This interpretation would indicate a change in the Sahul-Indian Ocean Bjercknes Mechanism (Di Nezio et al., 2016; Windler et al., 2019) with the 900-ka event, may have contributed to the observed productivity patterns at Site U1460.

The “Sahul-Indian Ocean Bjercknes Mechanism” amplifies changes in Indian Ocean atmospheric circulation by increasing east-west SST gradients due to increased exposure of the Sahul shelf in northwestern Australia. Thus, this mechanism leads to a positive feedback with ocean dynamical processes amplifying externally forced climatic changes in the Indian Ocean during glacial sea level lowstands (Di Nezio et al., 2016). This feedback thus enhances upwelling and sea surface cooling in the LC region during sea level lowstands during late Pleistocene high-amplitude glacials (Di Nezio et al., 2016; Spooner et al., 2011; Stuet et al., 2019; Windler et al., 2019). The intensification of G-IG Sahul-Indian Ocean Bjercknes Mechanism variability with MIS 24–22 would have had major effects on the overall productivity and water mass conditions even during interglacials. Notably, our data shows that higher productivity and thus organic carbon burial persisted during post-900-ka event interglacials in the southeastern Indian Ocean. We

interpret the increase in productivity at ~900–850 ka as a permanent shallowing of the thermocline depth within the eastern Indian Ocean after MIS 22. A shallow thermocline may have also increased nutrient upwelling/mixing in the mid to low latitudes during higher wind activity on interannual scales (McClymont and Rosell-Mel , 2005; Petrick et al., 2018).

In line with this interpretation, the initial increase in TOC content in the sediment during MIS 23 at U 1460 (Fig. 4c) corresponds with changes in the upper water column structure of Deep Sea Drilling Project (DSDP) Site 214 located at c. 10°S latitude on the ninety-east ridge (Figs. 1 and 4i; Gupta et al., 2008). Gupta et al. (2008) interpret their data as reflective of changing monsoonal and trade wind patterns, resulting in a switch from thick mixed layer and deep thermocline conditions at Site 214 towards lower thermocline depths and reduced mixed layer conditions that had fully established by MIS 21. The authors provide evidence for this via a switch from abundant *Trilobatus sacculifer* and rare *Globorotalia menardii* abundances to rare *T. sacculifer* and abundant *Gr. menardii* during MIS 24–21 (Fig. 4i; Gupta et al., 2008). A short return to pre-900-ka conditions during early MIS 21 is indicated by a slight decrease in *Gr. menardii* numbers at Site 214, as well as a drop in TOC values in Site U1460. Around 850 ka (MIS 21e–g), there is an apparent increase in organic matter flux and thus productivity at U1460 (Fig. 4c–g), at a time when the planktonic foraminifer record at Site 214 shows an overall reduced thermocline depth through stable and relatively high *Gr. menardii* abundances. The *T. sacculifer* record shows higher variability that may reflect the increased upper water column and mixed layer variability after the MPT (Fig. 4i, Gupta et al., 2008).

The increased organic carbon flux at Site U1460 coincides with a ~30 p.p.m. drop in atmospheric CO<sub>2</sub> concentrations after the 900-ka event (H nisch et al., 2009). This pCO<sub>2</sub> reduction is contemporary with a global turnover in surface water primary producers and the extinction of benthic foraminifer taxa due to changing organic matter fluxes (Kender et al., 2016).

Our nannofossil abundance data also records the contemporary community shift in calcareous nannofossils towards the dominance of small *Gephyrocapsa* spp. after the 900-ka event (Fig. 3d; Kender et al., 2016; Marino et al., 2009). The fact that bloom-forming small *Gephyrocapsa* spp. only became dominant ~850–800 ka ago during MIS 21/20 (Kender et al., 2016), may explain the recorded increase in net coccolith flux during the MIS 21/20 sea level drop at U1460 (Fig. 3c). The recorded *Gephyrocapsa* spp. dominance, as well as the initial increase in overall nannofossil accumulation (Fig. 3), are contemporary with higher organic carbon burial (Fig. 4c–e) at U1460 and Site 214 surface water changes (Fig. 4i). These results show that the shift in coccolithophore communities to small, bloom-forming species was likely a response to higher nutrient levels in the surface ocean after the MPT, which consequently also increased APN-ARs (Fig. 4a).

Finally, the offset between total APN-ARs and alkenone MARS hints at varying contributions of individual alkenone producing nannofossil taxa towards total alkenone fluxes. In particular it appears likely that the dominant small *Gephyrocapsa* spp (Fig. 3c) do not contribute significantly to alkenone MARS at U1460. We further note that falling sea levels may also have forced coccolithophore-dominated phytoplankton communities further offshore, increasing the contribution of non-calcifying haptophytes to the standing stock (Feng et al., 2009; Hanson et al., 2007), which are also known alkenone producers (de Vargas et al., 2007; Liu et al., 2009; Shi et al., 2015; Unrein et al., 2014). A decrease in calcifying haptophytes may consequently also explain decreasing coccolith fluxes while alkenone fluxes remained high and even increased during MIS 20, 18, and 16 (Fig. 4g). Further studies based on full nannofossil assemblage data are necessary to fully constrain the

observed offset between nannofossil and alkenone accumulation rates.

Considering that seasonality is an important factor for the nutrient enrichment of the primarily oligotrophic LC (Feng et al., 2009; Moore et al., 2007; Ridgway and Godfrey, 2015; Thompson et al., 2011), we propose that the overall coccolith accumulation at U1460 reflects increased seasonality during the initial ice sheet build-up and thus high-latitude cooling between MIS 19/18 and MIS 17/16. Such a cooling would have strengthened the LC due to a deeper steric height gradient along Australia's west coast (Furue, 2019; Wijeratne et al., 2018). This increase resulted in higher LC eddy formation (Fig. 1; Furue, 2019; Waite et al., 2007a, 2007b) during the southern hemisphere autumn and winter when the LC is strongest (Feng et al., 2009; Stellema et al., 2019; Thompson et al., 2011). More LC eddies and potentially higher LC transport resulting from increasing latitudinal temperature gradients increased surface water productivity. This relationship between LC strength and LC productivity is also documented in modern observational data (Feng et al., 2009; Furnas, 2007; Koslow et al., 2008; Lenanton et al., 2009; Stellema et al., 2019; Thompson et al., 2011). To test this relationship for the MPT, we compare the SST gradient between tropical Site 806 (McClymont and Rosell-Mel , 2005) and subtropical Site 593 (McClymont et al., 2016) in the Pacific with our LC productivity data (Fig. S2). The close co-variation of SST gradients and TOC accumulation indicates that southern hemisphere gradients may indeed have had an impact on LC productivity over the MPT.

Higher interglacial LC activity after the MPT is further supported by evidence from benthic foraminifer assemblages (Gallagher et al., 2009) and contemporary La Ni a like conditions in the equatorial Pacific (e.g., McClymont and Rosell-Mel , 2005), which are known to cause strong LC activity (Feng et al., 2009; Furnas, 2007; He et al., 2021; Wijffels et al., 2008).

Overall, our data thus indicate that the highest LC activity, and thus coccolith flux, occurred during the glacial initiations following the 900-ka event (Fig. 4). We interpret this LC pattern as a result of relatively strong ITF connectivity on the Sahul shelf (e.g., Di Nezio et al., 2018) due to relatively high sea levels well above the ~45-m-threshold. Gradual cooling of the Pacific cold tongue (Mart nez Garcia et al., 2010; McClymont and Rosell-Mel , 2005) resulted in more La Ni a like conditions at the beginning of post-MPT-glacials, following MIS 21, 19, and 17, likely further exacerbating late interglacial/early glacial LC variability in conjunction with increasing high latitude cooling (De Vleeschouwer et al., 2017, 2019, 2019; Wijeratne et al., 2018).

Dropping sea levels during continuous glacial cooling and ice sheet expansion would then have led to a restriction of the shallow ITF pathways sourcing the LC by exposing the Sahul Shelf in northern Australia (Auer et al., 2019; Di Nezio et al., 2016, 2018; Petrick et al., 2019; Windler et al., 2019). This rerouting and potential weakening of the southward flow of warm oligotrophic LC waters (De Vleeschouwer et al., 2019; Petrick et al., 2019; Spooner et al., 2011) allowed increasing mid to high latitude winds (Lamy et al., 2019; Mart nez Garcia et al., 2009, 2011, 2009; Stuut et al., 2019) to overcome the LC during glacial times.

Thereby, these processes would have resulted in the intensification of (sub-)surface upwelling along the South West Shelf of Australia (e.g., Takahashi and Okada, 2000; Rousseaux et al., 2012) once sea levels at Site U1460 dropped below a threshold of 45 m below present-day sea level. Sea level lowstands and intensified upwelling consequently led to the highest net alkenone and organic matter fluxes at Site U1460 during glacials. In contrast, overall coccolith flux is more closely related to increasing seasonality during early high latitude cooling, which favors a more intense LC.

### 5.2.2. Cyclic response of low-mid latitude surface productivity during the MPT

Gaussian bandpass filters based on REDFIT and wavelet analysis (Fig. 5) of NGR-derived U content show an anti-phased relationship with the quasi-100-kyr period (centered on 80 kyr and 125 kyr) of the ODP Site 1123 sea-level reconstructions (Fig. 6; Elderfield et al., 2012). We apply U accumulation rates as a high-resolution and remineralization resistant proxy for organic matter flux at Site U1460 (see Section 4.2.1; Auer et al., 2016). Although we show precession filters for reference (Fig. 6), our tuning of small *Gephyrocapsa* spp. to the SITIG precludes a direct interpretation of the precessional signal within our records, as it would result in circular reasoning.

We assume that the long-term variability of U and thus organic matter flux is caused by changing productivity at Site U1460 due to G-IG variability after the 900-ka event. This inverse relationship intensifies after the 900-ka event, as reflected by the increase in the 100-kyr amplitude of U during MIS 21 (Figs. 5 and 6b). This amplitude increase occurs at the same time when the quasi-100-kyr frequencies begin to dominate both sea level and climate (e.g., Maslin and Brierley, 2015). We consider this pattern a result of the Sahul-Indian Ocean Bjerknæs Mechanism due to glacial sea level falls affecting the eastern Indian Ocean (Di Nezio et al., 2016, 2018; Windler et al., 2019). These climatic effects linked to sea level were transferred southward toward Site U1460 from the ITF region by a reduced flow of warm, oligotrophic LC waters along the southwest shelf of Australia (Spooner et al., 2011; Petrick et al., 2019).

An increase in the 41-kyr-frequency amplitude of U, representing the influence of orbital obliquity on organic matter flux at Site U1460, is also discernible (Figs. 5b and 6b). Our analysis shows that while the obliquity imprint on sea level at Site 1123 remains overall constant and in phase with orbital obliquity (Figs. 5c and 6c; Elderfield et al., 2012), the obliquity component of U exhibits an apparent increase in amplitude starting with the 900-ka event (MIS 24–22). The amplitude increase is accompanied by a phase shift from in-phase variation with obliquity to a strong anti-phase relationship after MIS 22 (Fig. 6b). The increasing obliquity signature of productivity patterns seems at odds with the global climate system's shift towards quasi-100-kyr G-IG cycles (Bates et al., 2014; Clark et al., 2006; Ford et al., 2016; Head and Gibbard, 2015; McClymont et al., 2013). However, numerous studies also reported a similarly strong influence of high-latitude obliquity in the southern hemisphere during the Pleistocene (Bajo et al., 2020; Caley et al., 2011; Lamy et al., 2019; Maslin and Brierley, 2015).

We interpret this amplitude increase and frequency shift towards the 41-kyr-signal as an increasing control of obliquity on organic matter fluxes and surface water plankton blooms at Site U1460 after the MPT. This increase in obliquity forcing is mirrored in the western Indian Ocean, where a persistent high latitude obliquity forcing is also recorded between 0 and 800 ka BP (Caley et al., 2011). We note similar patterns in both long-term G-IG-forcing in our spectral analyses of the small *Gephyrocapsa* spp. recorded as in the NGR derived U content. Besides the increase in amplitude after MIS 22 we also detect a substantial phase shift in the 41-kyr-obliquity signal in our record of small *Gephyrocapsa* spp. from in-phase variation to predominant anti-phase variation with orbital obliquity and a clear co-variation with U accumulation and thus organic carbon flux (Fig. 6). This imprint of high latitude-controlled productivity variation on bloom-forming opportunistic coccolith taxa confirms the impact of the MPT on nutrient fluxes in the ocean (e.g., Kender et al., 2016).

The observed amplitude patterns thus imply an increased polar control on primary productivity at Site U1460 (i.e., Raymo et al., 2006). This observation is further supported by a contemporaneous amplitude increase and phase shift in the 23-kyr filter of U

(Fig. 6b). Thus, our results hint at an increase in the climatic imprint of obliquity and potentially also a stronger northern hemisphere precessional and thus monsoonal control on LC productivity after the 900-ka event.

### 5.3. The effect of sea level change on local environmental conditions at site U1460

Shallow marine areas are particularly susceptible to environmental changes due to G-IG-related sea-level variability that impact nutrient cycling and marine biological production (e.g., Ren et al., 2017). Significant exposure of the Sahul (northern Australia) and Sunda (Indonesia) shelves (Auer et al., 2019; Di Nezio et al., 2016; Windler et al., 2019) results in cooling sea surface temperatures in the tropical eastern Indian Ocean (Di Nezio et al., 2016; Windler et al., 2019). This reduction of the inflow of warmer ITF waters was thus also transported south by the southward flowing LC, eventually reaching the mid-latitude Site U1460. Recent studies reveal that the LC SSTs exhibited significant G-IG variability after MIS 22 (Stuut et al., 2019). We consider these changes to be a result of cooling (Di Nezio et al., 2018; Windler et al., 2019) and thermocline changes (e.g., Gupta et al., 2008, Figs. 3 and 4) in the equatorial Indian Ocean during the intense glacials following MIS 22–24. While global cooling during glacials is high-latitude driven, regional cooling in the eastern Ocean is exacerbated by the “Sahul-Indian Ocean Bjerknæs Mechanism” proposed by Di Nezio et al. (2016).

It is noteworthy that cooling between MIS 22–24, including the failed termination of MIS 24–23 (Bajo et al., 2020), was comparatively muted in both U1460 TEX<sub>86</sub> (Fig. 3e; Petrick et al., 2019) as well as adjusted surface water  $\delta^{18}\text{O}_{G, \text{ruber}}$  (Fig. 3f; Stuut et al., 2019) records compared to later glacials MIS 20, 18, and 16. However, organic matter flux proxies at Site U1460 (Fig. 4) indicate that significant organic matter flux and productivity changes occurred at ~850 ka during MIS 21. Thus, these changes happen in the absence of large shifts in temperature and  $\delta^{18}\text{O}_{G, \text{ruber}}$  records (Petrick et al., 2019; Stuut et al., 2019, Fig. 3). This discrepancy would suggest that local changes in SSTs are not fully coupled to regional shifts in organic matter fluxes at Site U1460 during the MPT.

We assume that the prominent changes in U and thus organic matter flux are caused by changing productivity at Site U1460 due to G-IG variability during the MPT. This inverse relationship intensifies after the 900-ka event, as reflected by the increase in the 100-kyr amplitude of U during MIS 21 (Fig. 6b). This amplitude increase occurs at the same time when the quasi-100-kyr frequencies begin to dominate both sea level and climate (e.g., Maslin and Brierley, 2015). We consider this pattern a result of the Sahul-Indian Ocean Bjerknæs Mechanism due to glacial sea level fall affecting the eastern Indian Ocean (Di Nezio et al., 2016, 2018; Windler et al., 2019). These climatic effects linked to sea level were transferred southward toward Site U1460 from the ITF region by a reduced flow of warm, oligotrophic LC waters along the southwest shelf of Australia during glacial times (Spooner et al., 2011; Petrick et al., 2019).

### 5.4. The Leeuwin Undercurrent – a new tracer for high latitude forcing and nutrient cycling at U1460 after the MPT

The SAMW and AAIW represent an effective transport mechanism of nutrients throughout the low latitude oceans (Laufkötter and Gruber, 2018; Moore et al., 2018; Sarmiento et al., 2004; You, 1998). Thus, G-IG changes in the supply of nutrients via the SAMW may also affect mid to low-latitude shelf productivity.

The bottom water community changes at Site U1460 include

changes in siliceous sponge spicule accumulation (Gallagher et al., 2017, Fig. 7a) and shifts in benthic foraminifer assemblages (Haller et al., 2018). Both serve as proxies for LUC conditions and indicate that significant changes in bottom water conditions occurred over the MPT at Site U1460 (Fig. 7). In particular, we note a shift in benthic foraminifer assemblages during the MPT that Haller et al. (2018) had already observed (Fig. 7b). The authors interpreted this change in the foraminifer community as a decrease in overall nutrient flux after the MPT at Site U1460. However, their interpretation is not supported by the organic carbon flux and primary productivity data presented here (Fig. 4). Re-examining their foraminifer data (Fig. 7b), we find an increase in *Uvigerina* spp., detritivores adapted to feed on fresh organic matter, coupled with a decrease in facultative anaerobes such as *Trifarina bradyi* (Haller et al., 2018; Murray, 2006), after the 900-ka event.

We assume that cool, relatively fast-flowing, and oxygen-rich water masses affected benthic foraminifer assemblages after the MPT at Site U1460, as these assemblage changes occur at the same time as an increase in sponge spicule accumulation (Gallagher et al., 2017, Fig. 7a) during MIS 24–21. Increasing bottom water oxygenation is well-supported by the decrease in facultative anaerobic benthic foraminifers and the increase of suspension-feeding sponge communities that thrive in cool, oxygen-rich water masses (Alvarez et al., 2017; Fromont et al., 2012; Leys et al., 2007; Murray, 2006). Sponges, however, are not a good proxy for organic matter fluxes, as they are highly adapted filter feeders (Fromont et al., 2012; Reiswig, 1974) that do not necessarily require higher nutrient fluxes to proliferate. The increase in detritivores such as *Uvigerina* spp. after the MPT (Fig. 7b) nevertheless offers additional evidence for the noted increase in organic matter flux at Site U1460 during MIS 21 (Fig. 4). The low resolution of the available benthic foraminifer records unfortunately precludes direct correlation with G-IG changes over the studied interval and warrants further research.

Considering the modern oceanography of the region, we conclude that changes in benthic environmental conditions at Site U1460 indicate an increased influence of cool, oxygenated waters via the LUC following the 900-ka event. We note that local G-IG changes at Site U1460 are contemporary with a cooling of intermediate waters at DSDP Site 593 in the Tasman Sea (Fig. 5c; McClymont et al., 2016). At Site 593, a strong interglacial cooling in intermediate water depths occurs with MIS 20 at the same time as sponge spicule accumulation at Site U1460 increases sharply with respect to pre-900-ka event patterns (Fig. 7a). The northward migration of the sub-Antarctic and subtropical frontal system thus resulted in a stepwise increase in the southern SAMW influx at Site 593 by MIS 20 and a contemporary intensification of the LUC at Site U1460. We, therefore, interpret the proliferation of extensive siliceous spicule producing sponges as an indicator for higher dissolved silica saturation (Maldonado et al., 2020) at Site U1460 as a direct result of higher SAMW influx via the LUC.

We, nevertheless, note that sea level (Fig. 7d) exerted a strong influence on the bottom water conditions at Site U1460, resulting in G-IG changes in the accumulation of sponge spicules after the 900-ka event. The changing sea levels may have led to a basinward migration of the LC/LUC current system with the higher amplitude (i.e., >45 m below present; see red line in Fig. 7d) sea level lowstands that initiated with MIS 24–22, as well as an increase in available hardground habitats for sponges (Fromont et al., 2012; Deik et al., 2019). However, the overall rise in sponge spicules with MIS 20 cannot be explained by sea level changes alone and is probably related to the LUC's proposed cooling. The close correlation of the XRF based biogenic silica (and thus sponge spicule) accumulation proxy at Site U1460 with the ODP Site 1123  $\delta^{13}\text{C}$  record (Fig. 5e) of Elderfield et al. (2012) further indicates a co-

variation of the LUC with G-IG changes in the carbon cycle (e.g., Elderfield et al., 2012). We relate this co-variation to changes in deep and conversely intermediate water formation in the Southern Ocean that affected both the formation and northward migration of intermediate (AAIW/SAMW) water masses. The bottom water changes at U1460 are thus directly related to an increase in deep-water ventilation and mixing as an expression of deep ocean carbon reservoir changes as described by Elderfield et al. (2012) and Farmer et al. (2019) based on deep water  $\delta^{13}\text{C}$  records.

## 6. Conclusions

Our data reveal significant productivity changes at Site U1460 over the MPT, which we interpret in the context of varying nutrient conditions within the LC/LUC system. The inferred shift in the LC/LUC current dynamics is the direct result of a series of oceanographic processes occurring across the 900-ka event:

- 1) Surface water primary productivity and organic carbon fluxes at Site U1460 increased significantly during MIS 21 due to increased nutrient availability and thermocline shoaling, LC eddy formation, and nutricline mixing.
- 2) Changes in Site U1460 upwelling at the rhythm of global G-IG cycles are predominantly controlled by the sea-level influence on LC strength and changing southern hemisphere temperature gradients after the 900-ka event. The latter led to increased wind-driven upwelling of cool, nutrient-rich lower thermocline waters during glacials.
- 3) The high-amplitude sea level cycles after the 900-ka event contributed to an apparent decoupling of alkenone/productivity and nanofossil fluxes. This decoupling observed at U1460 warrants further scrutiny as it may have also impacted other similar locations/sites.
- 4) The increasing influence of the 41-kyr obliquity cycle and an inferred stronger northern hemisphere precession control on surface water productivity reveals the increased climatic and environmental influence of high latitude G-IG processes along the western Australian shelf after the 900-ka event.
- 5) These local productivity changes may have resulted from an increased SAMW supply to Australia's west coast after the 900-ka event. This hypothesis is supported by observed changes in benthic communities at Site U1460 and the contemporary cooling of intermediate waters in the Tasman Sea.

Our data thus show that organic matter fluxes at Site U1460 were affected by the combined effect of sea level and oceanographic changes across the 900-ka event. In the post-900-ka event world, glacial upwelling and nutrient cycling changes on shelf areas resulted in an increased burial of organic carbon at Site U1460. We consider enhanced organic matter burial during glacials an important expression of the reorganized ocean-atmosphere system during the MPT. We thus conclude that changes in glacial organic carbon storage on the Earth's shelf regions warrant further scrutiny, particularly in the context of post-MPT climatic feedback mechanisms, as the overall impact of organic carbon burial on shelves is still poorly constrained, even during the most recent glacials.

## Author contribution

GA designed the study, generated and analyzed the data, wrote the manuscript and drafted the figures; BP contributed data, assisted in interpretation, was involved during data discussion and edited the first draft of the manuscript; TY contributed data, assisted in interpretation and edited the manuscript; BLM, HT and DDV contributed data and/or taxonomic expertise, data

interpretation and edited the manuscript. **AMG** provided funding and lab capabilities, analytical and interpretative expertise and edited the final draft of the (original and revised) manuscript.

### Data availability

The data and age model generated for Site U1460 presented in this study are available on PANGAEA, <https://doi.org/10.1594/PANGAEA.928015> and are also available through the supplementary data associated with this manuscript.

### Declaration of competing interest

The authors declare that they have no known competing financial interests or personal relationships that could have appeared to influence the work reported in this paper.

### Acknowledgments

This work utilized data provided by the International Ocean Discovery Program (IODP). All shipboard data are publicly available online from [www.iodp.tamu.edu](http://www.iodp.tamu.edu). We thank the D/V JOIDES Resolution staff and crew for their work during IODP Expedition 356 and the shipboard science party for generating all shipboard data. Y. Yoshikawa (JAMSTEC) and C. Puschenjak (University of Graz) are thanked for their assistance with sample preparation and analyses. This study was funded by JSPS (Japan Society for the Promotion of Science) Grant 17H07412 awarded to G. A. and contributes towards the DFG (German Science Foundation) project 320220579 awarded to Lars Reuning. David De Vleeschouwer was funded through the Cluster of Excellence “The Ocean Floor – Earth’s Uncharted Interface”. We would like to thank two anonymous reviewers and our editors for their many helpful suggestions. Timothy Horscroft (Elsevier) and Antje H. L. Voelker (IPMA; CCMAR) are thanked in particular for their invitation to write this paper and for their encouragement and considerable patience during the writing process. The authors declare no competing financial or nonfinancial interests.

### Appendix A. Supplementary data

Supplementary data to this article can be found online at <https://doi.org/10.1016/j.quascirev.2021.106965>.

### References

Alvarez, B., Frings, P.J., Clymans, W., Fontorbe, G., Conley, D.J., 2017. Assessing the potential of sponges (*Porifera*) as indicators of ocean dissolved Si concentrations. *Front. Mar. Sci.* 4, 149. <https://doi.org/10.3389/fmars.2017.00373>.

Anderson, R.F., 1982. Concentration, vertical flux, and remineralization of particulate uranium in seawater. *Geochem. Cosmochim. Acta* 46, 1293–1299. [https://doi.org/10.1016/0016-7037\(82\)90013-8](https://doi.org/10.1016/0016-7037(82)90013-8).

Anderson, R.F., Chase, Z., Fleisher, M.Q., Sachs, J., 2002. The Southern Ocean’s biological pump during the last glacial maximum. *Deep-Sea Res. Pt. II* 49, 1909–1938. [https://doi.org/10.1016/S0967-0645\(02\)00018-8](https://doi.org/10.1016/S0967-0645(02)00018-8).

Auderet, A., Schmitt, M., Martínez García, A., 2020. Simultaneous extraction and chromatographic separation of n-alkanes and alkenones from glycerol dialkyl glycerol tetraethers via selective Accelerated Solvent Extraction. *Org. Geochem.* 143, 103979 <https://doi.org/10.1016/j.orggeochem.2020.103979>.

Auer, G., De Vleeschouwer, D., Smith, R.A., Bogus, K., Groeneveld, J., Grunert, P., Castañeda, I.S., Petrick, B., Christensen, B., Fulthorpe, C., Gallagher, S.J., Henderiks, J., 2019. Timing and pacing of Indonesian throughflow restriction and its connection to Late Pliocene climate shifts. *Paleoceanog. Paleoclimatol.* 34, 635–657. <https://doi.org/10.1029/2018PA003512>.

Auer, G., Hauenberger, C.A., Reuter, M., Piller, W.E., 2016. Orbitally paced phosphogenesis in Mediterranean shallow marine carbonates during the middle Miocene Monterey event. *Geochem. Geophys. Geosyst.* 17, 1492–1510. <https://doi.org/10.1002/2016GC006299>.

Backman, J., Raffi, I., Rio, D., Fornaciari, E., Pälike, H., 2012. Biozonation and chronology of Miocene through Pleistocene calcareous nannofossils from low

and middle latitudes. *Newsl. Stratigr.* 45, 221–244. <https://doi.org/10.1127/0078-0421/2012/0022>.

Bajo, P., Drysdale, R.N., Woodhead, J.D., Hellstrom, J.C., Hodell, D., Ferretti, P., Voelker, A.H.L., Zanchetta, G., Rodrigues, T., Wolff, E., Tyler, J., Frisia, S., Spötl, C., Fallick, A.E., 2020. Persistent influence of obliquity on ice age terminations since the Middle Pleistocene transition. *Science* 367, 1235–1239. <https://doi.org/10.1126/science.aaw1114>.

Bates, S.L., Siddall, M., Waelbroeck, C., 2014. Hydrographic variations in deep ocean temperature over the mid-Pleistocene transition. *Quat. Sci. Rev.* 88, 147–158. <https://doi.org/10.1016/j.quascirev.2014.01.020>.

Bordiga, M., Bartol, M., Henderiks, J., 2015. Absolute nannofossil abundance estimates: quantifying the pros and cons of different techniques. *Rev. Micropaleontol.* 58, 155–165. <https://doi.org/10.1016/j.revmic.2015.05.002>.

Bosmans, J.H.C., Hilgen, F.J., Tuenter, E., Lourens, L.J., 2015. Obliquity forcing of low-latitude climate. *Clim. Past.* <https://doi.org/10.5194/cp-11-1335-2015>.

Brandano, M., Lipparini, L., Campagnoni, V., Tomassetti, L., 2012. Downslope-migrating large dunes in the Chattian carbonate ramp of the Majella mountains (central apennines, Italy). *Sediment. Geol.* 255–256, 29–41. <https://doi.org/10.1016/j.sedgeo.2012.02.002>.

Bull, Sen, C.Y., van Sebille, E., 2016. Sources, fate, and pathways of Leeuwin Current water in the Indian Ocean and Great Australian Bight: a Lagrangian study in an eddy-resolving ocean model. *J. Geophys. Res.: Oceans* 121, 1626–1639. <https://doi.org/10.1002/2015JC011486>.

Caley, T., Kim, J.H., Malaizé, B., Giraudeau, J., Laepple, T., Caillon, N., Charlier, K., Rebaubier, H., Rossignol, L., Castañeda, I.S., Schouten, S., Sinninghe Damsté, J.S., 2011. High-latitude obliquity as a dominant forcing in the Agulhas current system. *Clim. Past* 7, 1285–1296.

Chalk, T.B., Hain, M.P., Foster, G.L., Rohling, E.J., Sexton, P.F., Badger, M.P.S., Cherry, S.G., Hasenfratz, A.P., Haug, G.H., Jaccard, S.L., Martínez García, A., Pälike, H., Pancost, R.D., Wilson, P.A., 2017. Causes of ice age intensification across the Mid-Pleistocene Transition. *Proc. Natl. Acad. Sci. U.S.A.* 114, 13114–13119. <https://doi.org/10.1073/pnas.1702143114>.

Chase, Z., Anderson, R.F., Fleisher, M.Q., 2001. Evidence from authigenic uranium for increased productivity of the glacial subantarctic ocean. *Paleoceanography* 16, 468–478. <https://doi.org/10.1038/nature03544>.

Clark, P.U., Archer, D., Pollard, D., Blum, J.D., Rial, J.A., Brovkin, V., Mix, A.C., Pisias, N.G., Roy, M., 2006. The middle Pleistocene transition: characteristics, mechanisms, and implications for long-term changes in atmospheric pCO<sub>2</sub>. *Quat. Sci. Rev.* 25, 3150–3184. <https://doi.org/10.1016/j.quascirev.2006.07.008>.

Crucifix, M., Loutre, M.F., Berger, A., 2006. The climate response to the astronomical forcing. *Space Sci. Rev.* 125, 213–226. <https://doi.org/10.1007/s11214-006-9058-1>.

de Vargas, C., Aubry, M.-P., Probert, I., Young, J., 2007. Chapter 12 - origin and evolution of coccolithophores: from coastal hunters to oceanic farmers. In: Falkowski, P.G., Knoll, A.H. (Eds.), *Evolution of Primary Producers in the Sea*. Evolution of Primary Producers in the Sea. Academic Press, Burlington, pp. 251–285. <https://doi.org/10.1016/B978-012370518-1/50013-8>.

De Vleeschouwer, D., Dunlea, A.G., Auer, G., Anderson, C.H., Brumsack, H., de Loach, A., Gurnis, M., Huh, Y., Ishiwa, T., Jang, K., Kominz, M.A., März, C., Schnetger, B., Murray, R.W., Pälike, H., scientists, E.3.S., 2017. Quantifying K, U, and Th contents of marine sediments using shipboard natural gamma radiation spectra measured on DV JOIDES Resolution. *Geochem. Geophys. Geosyst.* 18, 1053–1064. <https://doi.org/10.1002/2016GC006715>.

De Vleeschouwer, D., Petrick, B.F., Martínez García, A., 2019. Stepwise weakening of the Pliocene Leeuwin current. *Geophys. Res. Lett.* 46, 8310–8319. <https://doi.org/10.1029/2019GL083670>.

Deik, H., Reuning, L., Petrick, B., Takayanagi, H., 2019. Hardened faecal pellets as a significant component in deep water, subtropical marine environments. *The Depositional Record* 26, 845. <https://doi.org/10.1002/dep2.64>.

Deik, H., Reuning, L., Courtillot, M., Petrick, B., Bassetti, M., 2021. The sedimentary record of Quaternary glacial to interglacial sea-level change on a subtropical carbonate ramp: southwest Shelf of Australia. *Sedimentology* 68, 593–608. <https://doi.org/10.1111/sed.12793>.

Di Nezio, P.N., Timmermann, A., Tierney, J.E., Jin, F.-F., Otto-Bliesner, B., Rosenbloom, N., Mapeo, B., Neale, R., Ivanovic, R.F., Montenegro, A., 2016. The climate response of the Indo-Pacific warm pool to glacial sea level. *Paleoceanography* 31, 866–894. <https://doi.org/10.1002/2015PA002890>.

Di Nezio, P.N., Tierney, J.E., Otto-Bliesner, B.L., Timmermann, A., Bhattacharya, T., Rosenbloom, N., Brady, E., 2018. Glacial changes in tropical climate amplified by the Indian Ocean. *Sci. Adv.* 4, eaat9658 <https://doi.org/10.1126/sciadv.aat9658>.

Domingues, C.M., Maltrud, M.E., Wijffels, S.E., Church, J.A., Tomczak, M., 2007. Simulated Lagrangian pathways between the Leeuwin current system and the upper-ocean circulation of the southeast Indian ocean. *Deep-Sea Res. Pt. II* 54, 797–817.

Doveton, J.H., 1991. Lithofacies and geochemical facies profiles from nuclear wire-line logs: new subsurface templates for sedimentary modeling. *Kansas Geological Survey, Bulletin* 233, 101–110.

Elderfield, H., Ferretti, P., Greaves, M., Crowhurst, S., McCave, I.N., Hodell, D., Piotrowski, A.M., 2012. Evolution of ocean temperature and ice volume through the mid-Pleistocene climate transition. *Science* 337, 704–709. <https://doi.org/10.1126/science.1221294>.

Farmer, J.R., Hönisch, B., Haynes, L.L., Kroon, D., Jung, S., Ford, H.L., Raymo, M.E., Jaume-Seguí, M., Bell, D.B., Goldstein, S.L., Pena, L.D., Yehudai, M., Kim, J., 2019. Deep Atlantic Ocean carbon storage and the rise of 100,000-year glacial cycles. *Nat. Geosci.* 12, 355–360. <https://doi.org/10.1038/s41561-019-0334-6>.

- Feng, F., Bailer-Jones, C.A.L., 2015. Obliquity and precession as pacemakers of Pleistocene deglaciations. *Quat. Sci. Rev.* 122, 166–179. <https://doi.org/10.1016/j.quascirev.2015.05.006>.
- Feng, M., Waite, A., Thompson, P., 2009. Climate variability and ocean production in the Leeuwin Current system off the west coast of Western Australia. *J. Roy. Soc. West Aust.* 92 (2), 67–81.
- Fine, R.A., 1993. Circulation of antarctic intermediate water in the south Indian ocean. *Deep-Sea Res. Pt. I* 40, 2021–2042. [https://doi.org/10.1016/0967-0637\(93\)90043-3](https://doi.org/10.1016/0967-0637(93)90043-3).
- Ford, H.L., Sosdian, S.M., Rosenthal, Y., Raymo, M.E., 2016. Gradual and abrupt changes during the mid-pleistocene transition. *Quat. Sci. Rev.* 148, 222–233.
- Fromont, J., Althaus, F., McEnulty, F.R., Williams, A., Salotti, M., Gomez, O., Gowlett-Holmes, K., 2012. Living on the edge: the sponge fauna of Australia's south-western and northwestern deep continental margin. In: Maldonado, M., Turon, X., Becerro, M., Jesús Uriz, M. (Eds.), *Ancient Animals, New Challenges: Developments in Sponge Research*. Springer Netherlands, Dordrecht, pp. 127–142. [https://doi.org/10.1007/978-94-007-4688-6\\_12](https://doi.org/10.1007/978-94-007-4688-6_12).
- Furnas, M., 2007. Intra-seasonal and inter-annual variations in phytoplankton biomass, primary production and bacterial production at North West Cape, Western Australia: links to the 1997–1998 El Niño event. *Continent. Shelf Res.* 27, 958–980.
- Furue, R., 2019. The three-dimensional structure of the Leeuwin Current System in density coordinates in an eddy-resolving OGCM. *Ocean Model.* 138, 36–50. <https://doi.org/10.1016/j.ocemod.2019.03.001>.
- Furue, R., Guerreiro, K., Phillips, H.E., Julian P McCreary, J., Bindoff, N.L., 2017. On the Leeuwin Current system and its linkage to zonal flows in the South Indian Ocean as inferred from a gridded hydrography. *J. Phys. Oceanogr.* 47, 583–602. <https://doi.org/10.1175/JPO-D-16-0170.1>.
- Furue, R., McCreary, J.P., Benthuyens, J., Phillips, H.E., Bindoff, N.L., 2013. Dynamics of the Leeuwin Current: Part 1. Coastal flows in an inviscid, variable-density, layer model. *Dynam. Atmos. Oceans* 63, 24–59. <https://doi.org/10.1016/j.jdynatmoce.2013.03.003>.
- Gallagher, S.J., Fulthorpe, C.S., Bogus, K., Auer, G., Baranwal, S., Castañeda, I.S., Christensen, B.A., De Vleeschouwer, D., Franco, D.R., Groeneveld, J., Gurnis, M., Haller, C., He, Y., Henderiks, J., Himmler, T., Ishiwa, T., Iwatani, H., Jatiningrum, R.S., Kominz, M.A., Korpany, C.A., Lee, E.Y., Levin, E., Mamo, B.L., McGregor, H.V., McHugh, C.M., Petrick, B.F., Potts, D.C., Rastegar Lari, A., Renema, W., Reuning, L., Takayanagi, H., Zhang, W., 2017. Site U1460. Expedition 356 Scientists. In: Gallagher, S.J., Fulthorpe, C.S. (Eds.), *Proceedings of the International Ocean Discovery Program*. International Ocean Discovery Program. <https://doi.org/10.14379/iodp.proc.356.101.2017>.
- Gallagher, S.J., Wallace, M.W., Li, C.L., Kinna, B., Bye, J.T., Akimoto, K., Torii, M., 2009. Neogene history of the west pacific warm pool, kuroshio and Leeuwin currents. *Paleoceanography* 24, 1–27. <https://doi.org/10.1029/2008PA001660>.
- Gattuso, J.P., Gentili, B., Duarte, C.N.M., Kleypas, J.N.A., Middelburg, J.N.J., Antoine, D., 2006. Light availability in the coastal ocean: impact on the distribution of benthic photosynthetic organisms and their contribution to primary production. *Biogeosciences* 3, 489–513. <https://doi.org/10.5194/bg-3-489-2006>.
- Gupta, A.K., Sundar Raj, M., Mohan, K., De, S., 2008. A major change in monsoon-driven productivity in the tropical Indian Ocean during ca 1.2–0.9 Myr: foraminiferal faunal and stable isotope data. *Palaeogeogr. Palaeoclimatol. Palaeoecol.* 261, 234–245. <https://doi.org/10.1016/j.palaeo.2008.01.012>.
- Haller, C., Hallock, P., Hine, A.C., Smith, C.G., 2018. Benthic foraminifera from the Carnarvon ramp reveal variability in Leeuwin current activity (western Australia) since the Pliocene. *Mar. Micropaleontol.* 142, 25–39. <https://doi.org/10.1016/j.marmicro.2018.05.005>.
- Hammer, Ø., Harper, D.A.T., Ryan, P.D., 2001. PAST: paleontological statistics software package for education and data analysis. *Palaeontol. Electron.* 4, 1–9.
- Hanson, C.E., Waite, A.M., Thompson, P.A., Pattiaratchi, C.B., 2007. Phytoplankton community structure and nitrogen nutrition in Leeuwin Current and coastal waters off the Gascoyne region of Western Australia. The Leeuwin Current and its Eddies 54, 902–924. <https://doi.org/10.1016/j.dsr2.2006.10.002>.
- Hasenfratz, A., Jaccard, S., Garcia, A., Sigman, D., Hodell, D., Vance, D., Bernasconi, S., Kleiven, H., Haumann, F., Haug, G., 2019. The residence time of Southern Ocean surface waters and the 100,000-year ice age cycle. *Science* 363 (6431), 1080–1084. <https://doi.org/10.1126/science.aat7067>.
- He, Y., Wang, H., Liu, Z., 2021. Development of the Leeuwin current on the north-west shelf of Australia through the pliocene-pleistocene period. *Earth Planet Sci. Lett.* 559, 116767. <https://doi.org/10.1016/j.epsl.2021.116767>.
- Head, M.J., Gibbard, P.L., 2015. Early–Middle Pleistocene transitions: linking terrestrial and marine realms. *Quat. Int.* 389, 7–46. <https://doi.org/10.1016/j.quaint.2015.09.042>.
- Holbourn, A., Kuhnt, W., Kawamura, H., Jian, Z., Grootes, P., Erlenkeuser, H., Xu, J., 2005. Orbitally paced paleoproductivity variations in the Timor Sea and Indonesian Throughflow variability during the last 460 kyr. *Paleoceanography* 20, PA3002. <https://doi.org/10.1029/2004PA001094>.
- Hönisch, B., Hemming, N.G., Archer, D., Siddall, M., McManus, J.F., 2009. Atmospheric carbon dioxide concentration across the mid-Pleistocene transition. *Science* 324, 1551–1554. <https://doi.org/10.1126/science.1171477>.
- Huybers, P., Wunsch, C., 2005. Obliquity pacing of the late Pleistocene glacial terminations. *Nature* 434, 491–494. <https://doi.org/10.1038/nature03401>.
- Kawamura, H., Holbourn, A., Kuhnt, W., 2006. Climate variability and land–ocean interactions in the Indo Pacific Warm Pool: a 460-ka palynological and organic geochemical record from the Timor Sea. *Mar. Micropaleontol.* 59, 1–14. <https://doi.org/10.1016/j.marmicro.2005.09.001>.
- Kemp, A.E.S., Grigorov, I., Pearce, R.B., Naveira Garabato, A.C., 2010. Migration of the Antarctic Polar Front through the mid-Pleistocene transition: evidence and climatic implications. *Quat. Sci. Rev.* 29, 1993–2009. <https://doi.org/10.1016/j.quascirev.2010.04.027>.
- Kender, S., McClymont, E.L., Elmore, A.C., Emanuele, D., Leng, M.J., Elderfield, H., 2016. Mid Pleistocene foraminiferal mass extinction coupled with phytoplankton evolution. *Nat. Commun.* 7, 11970. <https://doi.org/10.1038/ncomms11970>.
- Kender, S., Ravelo, A.C., Worne, S., Swann, G.E.A., Leng, M.J., Asahi, H., Becker, J., Detlef, H., Aiello, I.W., Andreasen, D., Hall, I.R., 2018. Closure of the bering strait caused mid-pleistocene transition cooling. *Nat. Commun.* 9, 173. <https://doi.org/10.1038/s41467-018-07828-0>.
- Koch-Larrouy, A., Morrow, R., Penduff, T., Juza, M., 2010. Origin and mechanism of subantarctic mode water formation and transformation in the southern Indian ocean. *Ocean Dynam.* 60, 563–583. <https://doi.org/10.1007/s10236-010-0276-4>.
- Koslow, J.A., Pesant, S., Feng, M., Pearce, A., Fearn, P., Moore, T., Matear, R., Waite, A., 2008. The effect of the Leeuwin Current on phytoplankton biomass and production off Southwestern Australia. *J. Geophys. Res.* 113, 9145. <https://doi.org/10.1029/2007JC004102>.
- Ku, T.-L., Knauss, K.G., Mathieu, G.G., 1977. Uranium in open ocean: concentration and isotopic composition. *Deep Sea Res.* 24, 1005–1017. [https://doi.org/10.1016/0146-6291\(77\)90571-9](https://doi.org/10.1016/0146-6291(77)90571-9).
- Kunkelova, T., Jung, S.J.A., de Leau, E.S., Odling, N., Thomas, A.L., Betzler, C., Eberli, G.P., Alvarez-Zarikian, C.A., Alonso-García, M., Bialik, O.M., Blättler, C.L., Guo, J.A., Haffens, S., Horozal, S., Mee, A.L.H., Inoue, M., Jovane, L., Lanci, L., Laya, J.C., Lüdmann, T., Bejunga, N.N., Nakakuni, M., Niino, K., Petruny, L.M., Pratiwi, S.D., Reijmer, J.J.G., Reolid, J., Slagle, A.L., Sloss, C.R., Su, X., Swart, P.K., Wright, J.D., Yao, Z., Young, J.R., Lindhorst, S., Stainbank, S., Rueggeberg, A., Spezzaferri, S., Carrasqueira, I., Yu, S., Kroon, D., 2018. A two million year record of low-latitude aridity linked to continental weathering from the Maldives. *Prog. Earth Planet. Sci.* 5, 86.
- Lamy, F., Chiang, J.C.H., Martínez-Méndez, G., Thierens, M., Arz, H.W., Bosmans, J., Hebbeln, D., Lambert, F., Lembke-Jene, L., Stuut, J.-B., 2019. Precession modulation of the South Pacific westerly wind belt over the past million years. *Proc. Natl. Acad. Sci. U.S.A.* 116, 23455–23460. <https://doi.org/10.1073/pnas.1905847116>.
- Laskar, J., Robutel, P., Joutel, F., Gastineau, M., Correia, A.C.M., Levrard, B., 2004. A long-term numerical solution for the insolation quantities of the Earth. *Astron. Astrophys.* 428, 261–285. <https://doi.org/10.1051/0004-6361/20041335>.
- Laufkötter, C., Gruber, N., 2018. Will marine productivity wane? *Science* 359, 1103–1104. <https://doi.org/10.1126/science.aat0795>.
- Lenanton, R.C., Caputi, N., Kangas, M., Craine, M., 2009. The ongoing influence of the Leeuwin Current on economically important fish and invertebrates off temperate Western Australia—has it changed? *J. Roy. Soc. West Aust.* 92, 111–127.
- Leys, S.P., Mackie, G.O., Reiswig, H.M., 2007. The biology of glass sponges. In: *Advances in Marine Biology, Advances in Marine Biology*. Academic Press, pp. 1–145. [https://doi.org/10.1016/S0065-2881\(06\)52001-2](https://doi.org/10.1016/S0065-2881(06)52001-2).
- Lisiecki, L.E., Raymo, M.E., 2005. A Pliocene–Pleistocene stack of 57 globally distributed benthic  $\delta^{18}\text{O}$  records. *Paleoceanography* 20, 1–17. <https://doi.org/10.1029/2004PA001071>.
- Liu, H., Probert, I., Uitz, J., Claustre, H., Aris-Brosou, S., Frada, M., Not, F., de Vargas, C., 2009. Extreme diversity in non-calcifying haptophytes explains a major pigment paradox in open oceans. *Proc. Natl. Acad. Sci. U.S.A.* 106, 12803–12808. <https://doi.org/10.1073/pnas.0905841106>.
- Lupi, C., Bordiga, M., Cobiainchi, M., 2012. Geophycocapsa occurrence during the middle Pleistocene transition in the northern Pacific Ocean. *Shatsky Rise) Geobios* 45 (2), 209–217. <https://doi.org/10.1016/j.geobios.2011.04.001>.
- Maldonado, M., López-Acosta, M., Beazley, L., Kenchington, E., Koutsouveli, V., Riesgo, A., 2020. Cooperation between passive and active silicon transporters clarifies the ecophysiology and evolution of biosilicification in sponges. *Sci Adv* 6, eaba9322. <https://doi.org/10.1126/sciadv.aba9322>.
- Marino, M., Maiorano, P., Lirer, F., Pelosi, N., 2009. Response of calcareous nannofossil assemblages to paleoenvironmental changes through the mid-Pleistocene revolution at Site 1090 (Southern Ocean). *Palaeogeogr. Palaeoclimatol. Palaeoecol.* 280, 333–349. <https://doi.org/10.1016/j.palaeo.2009.06.019>.
- Martínez García, A., Rosell-Melé, A., Geibert, W., Gersonde, R., Masqué, P., Gaspari, V., Barbante, C., 2009. Links between iron supply, marine productivity, sea surface temperature, and CO<sub>2</sub> over the last 1.1 Ma. *Paleoceanography* 24, PA1207. <https://doi.org/10.1029/2008PA001657>.
- Martínez García, A., Rosell-Melé, A., Jaccard, S.L., Geibert, W., Sigman, D.M., Haug, G.H., 2011. Southern Ocean dust–climate coupling over the past four million years. *Nature* 476, 312–315. <https://doi.org/10.1038/nature10310>.
- Martínez García, A., Rosell-Melé, A., McClymont, E.L., Gersonde, R., Haug, G.H., 2010. Subpolar link to the emergence of the modern Equatorial Pacific cold tongue. *Science* 328, 1550–1553. <https://doi.org/10.1126/science.1184480>.
- Maslin, M.A., Brierley, C.M., 2015. The role of orbital forcing in the early middle Pleistocene transition. *Quat. Int.* 389, 47–55. <https://doi.org/10.1016/j.quaint.2015.01.047>.
- McClymont, E.L., Rosell-Melé, A., 2005. Links between the onset of modern Walker circulation and the mid-Pleistocene climate transition. *Geology* 33, 389. <https://doi.org/10.1130/G21292.1>.
- McClymont, E.L., Sosdian, S.M., Rosell-Melé, A., Rosenthal, Y., 2013. Pleistocene sea-surface temperature evolution: early cooling, delayed glacial intensification, and implications for the mid-Pleistocene climate transition. *Earth Sci. Rev.* 123,

- 173–193. <https://doi.org/10.1016/j.earscirev.2013.04.006>.
- McClymont, E.L., Elmore, A.C., Kender, S., Leng, M.J., Greaves, M., Elderfield, H., 2016. Pliocene-Pleistocene evolution of sea surface and intermediate water temperatures from the southwest Pacific. *Paleoceanography* 31, 895–913. <https://doi.org/10.1002/2016PA002954>.
- McCorkle, D.C., Veeh, H.H., Heggie, D.T., 1994. Glacial-holocene paleoproductivity off western Australia: a comparison of proxy records. In: *Carbon Cycling in the Glacial Ocean: Constraints on the Ocean's Role in Global Change, Quantitative Approaches in Paleoceanography*. Springer, Berlin, Heidelberg, Berlin, Heidelberg, pp. 443–479. [https://doi.org/10.1007/978-3-642-78737-9\\_20](https://doi.org/10.1007/978-3-642-78737-9_20).
- McManus, J., Berelson, W.M., Klinkhammer, G.P., Hammond, D.E., Holm, C., 2005. Authigenic uranium: relationship to oxygen penetration depth and organic carbon rain. *Geochim. Cosmochim. Acta* 69, 95–108. <https://doi.org/10.1016/j.gca.2004.06.023>.
- Meyers, S.R., 2014. *Astrochron: A Computational Tool for Astrochronology*. Middleton, J.F., Cirano, M., 2002. A northern boundary current along Australia's southern shelves: the Flinders Current. *J. Geophys. Res.: Oceans* 107, 12. <https://doi.org/10.1029/2000JC000701>, 1–12–11.
- Moore, J.K., Fu, W., Primeau, F., Britten, G.L., Lindsay, K., Long, M., Doney, S.C., Mahowald, N., Hoffman, F., Randerson, J.T., 2018. Sustained climate warming drives declining marine biological productivity. *Science* 359, 1139–1143. <https://doi.org/10.1126/science.aao6379>.
- Moore, T.S., Matear, R.J., Marra, J., Clementson, L., 2007. Phytoplankton variability off the Western Australian Coast: mesoscale eddies and their role in cross-shelf exchange. *The Leeuwin Current and its Eddies* 54, 943–960. <https://doi.org/10.1016/j.dsr2.2007.02.006>.
- Murray, J.W., 2006. *Ecology and Applications of Benthic Foraminifera*, first ed. Cambridge University Press, Cambridge.
- Okada, H., Wells, P., 1997. Late Quaternary nannofossil indicators of climate change in two deep-sea cores associated with the Leeuwin Current off Western Australia. *Palaeogeogr. Palaeoclimatol. Palaeoecol.* 131 (3–4), 413–432. [https://doi.org/10.1016/S0031-0182\(97\)00014-X](https://doi.org/10.1016/S0031-0182(97)00014-X).
- Pena, L.D., Goldstein, S.L., 2014. Thermohaline circulation crisis and impacts during the mid-Pleistocene transition. *Science* 345, 318–322. <https://doi.org/10.1126/science.1249770>.
- Perch-Nielsen, K., 1985. *Cenozoic calcareous nanofossils*. In: Bolli, H.M., Saunders, J.B., Perch-Nielsen, K. (Eds.), *Plankton Stratigraphy Volume 1*, vol. 1. Cambridge University Press, Cambridge, pp. 427–554.
- Petrick, B., McClymont, E.L., Littler, K., Rosell-Melé, A., Clarkson, M.O., Maslin, M., Röhl, U., Shevenell, A.E., Pancost, R.D., 2018. Oceanographic and climatic evolution of the southeastern subtropical Atlantic over the last 3.5 Ma. *Earth Planet. Sci. Lett.* 492 IS –, 12–21. <https://doi.org/10.1016/j.epsl.2018.03.054>.
- Petrick, B., Martínez García, A., Auer, G., Reuning, L., Auderset, A., Deik, H., Takayanagi, H., De Vleeschouwer, D., Iryu, Y., Haug, G.H., 2019. Glacial Indonesian throughflow weakening across the mid-pleistocene climatic transition. *Sci. Rep.* 9, 16995. <https://doi.org/10.1038/s41598-019-53382-0>.
- Raddadi, M.C., Arnaud Vanneau, A., Poupeau, G., Carrio-Schaffhauser, E., Arnaud, H., Rivera, A., 2005. Interpretation of gamma-ray logs: the distribution of uranium in carbonate platform. *Compt. Rendus Geosci.* 337, 1457–1461. <https://doi.org/10.1016/j.crte.2005.08.009>.
- Raffi, I., Backman, J., Fornaciari, E., Pälike, H., Rio, D., Lourens, L.J., Hilgen, F.J., 2006. A review of calcareous nannofossil astrochronology encompassing the past 25 million years. *Quat. Sci. Rev.* 25, 3113–3137. <https://doi.org/10.1016/j.quascirev.2006.07.007>.
- Railsback, L.B., Gibbard, P.L., Head, M.J., Voarintsoa, N.R.G., Toucanne, S., 2015. An optimized scheme of lettered marine isotope substages for the last 1.0 million years, and the climatostratigraphic nature of isotope stages and substages. *Quat. Sci. Rev.* 111, 94–106. <https://doi.org/10.1016/j.quascirev.2015.01.012>.
- Raymo, M.E., Lisiecki, L.E., Nisancioglu, K.H., 2006. Plio-pleistocene ice volume, antarctic climate, and the global 180 record. *Science* 313, 492–495. <https://doi.org/10.1126/science.1123296>.
- Reiswig, H.M., 1974. Water transport, respiration and energetics of three tropical marine sponges. *J. Exp. Mar. Biol. Ecol.* 14, 231–249. [https://doi.org/10.1016/0022-0981\(74\)90005-7](https://doi.org/10.1016/0022-0981(74)90005-7).
- Ren, H., Sigman, D.M., Martínez García, A., Anderson, R.F., Chen, M.-T., Ravelo, A.C., Straub, M., Wong, G.T.F., Haug, G.H., 2017. Impact of glacial/interglacial sea level change on the ocean nitrogen cycle. *Proc. Natl. Acad. Sci. U.S.A.* 114, E6759–E6766.
- Richardson, L.E., Middleton, J.F., Kyser, T.K., James, N.P., Opdyke, B.N., 2019. Shallow water masses and their connectivity along the southern Australian continental margin. *Deep-Sea Res. Pt. I* 152, 103083. <https://doi.org/10.1016/j.dsr.2019.103083>.
- Ridgway, K.R., Dunn, J.R., 2007. Observational evidence for a Southern Hemisphere oceanic supergyre. *Geophys. Res. Lett.* 34, L13612. <https://doi.org/10.1029/2007GL030392>.
- Ridgway, K.R., Godfrey, J.S., 2015. The source of the Leeuwin Current seasonality. *J. Geophys. Res.: Oceans* 120, 6843–6864. <https://doi.org/10.1002/2015JC011049>.
- Robinson, R.S., Jones, C.A., Kelly, R.P., Rafter, P., Etourneau, J., Martinez, P., 2019. A cool, nutrient-enriched eastern Equatorial Pacific during the mid-Pleistocene transition. *Geophys. Res. Lett.* 46, 2187–2195. <https://doi.org/10.1029/2018GL081315>.
- Ronge, T.A., Steph, S., Tiedemann, R., Prange, M., Merkel, U., Nürnberg, D., Kuhn, G., 2015. Pushing the boundaries: glacial/interglacial variability of intermediate and deep waters in the southwest Pacific over the last 350,000 years. *Paleoceanography* 30, 23–38. <https://doi.org/10.1002/2014PA002727>.
- Rosell-Fieschi, M., Rintoul, S.R., Gourrion, J., Pelegrí, J.L., 2013. Tasman Leakage of intermediate waters as inferred from Argo floats. *Geophys. Res. Lett.* 40, 5456–5460. <https://doi.org/10.1002/2013GL057797>.
- Rousseaux, C.S.G., Lowe, R., Feng, M., Waite, A.M., Thompson, P.A., 2012. The role of the Leeuwin Current and mixed layer depth on the autumn phytoplankton bloom off Ningaloo Reef, Western Australia. *Continental Shelf Res.* 32, 22–35. <https://doi.org/10.1016/j.csr.2011.10.010>.
- Ryan, W.B.F., Carbotte, S.M., Coplan, J.O., O'Hara, S., Melkonian, A., Arko, R., Weissel, R.A., Ferrini, V., Goodwillie, A., Natische, F., Bonczkowski, J., Zemsky, R., 2009. Global multi-resolution topography synthesis. G-cubed 10, Q03014. <https://doi.org/10.1029/2008GC002332>.
- Sarmiento, J.L., Gruber, N., Brzezinski, M.A., Dunne, J.P., 2004. High-latitude controls of thermocline nutrients and low latitude biological productivity. *Nature* 427, 56–60. <https://doi.org/10.1038/nature02127>.
- Sato, T., Takayama, T., 1992. A stratigraphically significant new species of the calcareous nannofossil *Reticulofenestra asanoi*. *Centenary Jpn. Micropaleontol.* 457–460.
- Schlosser, F., 2014. A dynamical model for the Leeuwin undercurrent. *J. Phys. Oceanogr.* 44, 1798–1810. <https://doi.org/10.1175/JPO-D-13-0226.1>.
- Schott, F.A., Xie, S.-P., McCreary Jr., J.P., 2009. Indian Ocean circulation and climate variability. *Rev. Geophys.* 47, 3295. <https://doi.org/10.1029/2007RG000245>.
- Schulz, M., Mudelsee, M., 2002. REDFIT: estimating red-noise spectra directly from unevenly spaced paleoclimatic time series. *Comput. Geosci.* 28, 421–426. [https://doi.org/10.1016/S0098-3004\(01\)00044-9](https://doi.org/10.1016/S0098-3004(01)00044-9).
- Shi, Q., Araie, H., Bakku, R.K., Fukao, Y., Rakwal, R., Suzuki, I., Shiraiwa, Y., 2015. Proteomic analysis of lipid body from the alkenone-producing marine haptophyte alga *Tisochrysis lutea*. *Proteomics* 15, 4145–4158. <https://doi.org/10.1002/pmic.201500010>.
- Sinnesael, M., Vleeschouwer, D.D., Zeeden, C., Batenburg, S.J., Silva, A.-C. da, Winter, N.J., de Dinarès-Turell, J., Drury, A.J., Gambacorta, G., Hilgen, F.J., Hinnov, L.A., Hudson, A.J.L., Kemp, D.B., Lantink, M.L., Laurin, J., Li, M., Liebrand, D., Ma, C., Meyers, S.R., Monkenbusch, J., Montanari, A., Nohl, T., Pälike, H., Pas, D., Ruhl, M., Thibault, N., Vahlenkamp, M., Valero, L., Wouters, S., Wu, H., Claeys, P., 2019. The Cyclostratigraphy Intercomparison Project (CIP): consistency, merits and pitfalls. *Earth Sci. Rev.* 1–68. <https://doi.org/10.1016/j.earscirev.2019.102965>.
- Speich, S., Blanke, B., de Vries, P., Drijfhout, S., Döös, K., Ganachaud, A., Marsh, R., 2002. Tasman leakage: a new route in the global ocean conveyor belt. *Geophys. Res. Lett.* 29, 55. <https://doi.org/10.1029/2001GL014586>.
- Spooner, M.I., De Deckker, P., Barrows, T.T., Fifield, L.K., 2011. The behaviour of the Leeuwin current offshore NW Australia during the last five glacial-interglacial cycles. *Global Planet. Change* 75, 119–132. <https://doi.org/10.1016/j.jglplacha.2010.10.015>.
- Stax, R., Stein, R., 1995. *Data report: organic carbon and carbonate records from detroit seamount and patton-murray seamount: results from sites 882 and 887 (North Pacific Transect)*. *Proc. Ocean Drill. Progr. Sci. Results* 145, 645–655.
- Stella, A., Gupta, Sen, A., Tschett, A.S., 2019. Projected slow down of South Indian Ocean circulation. *Sci. Rep.* 9, 17705. <https://doi.org/10.1038/s41598-019-54092-3>.
- Stuut, J.-B.W., De Deckker, P., Pellitero, M.S., Bassinot, F., Drury, A.J., Walczak, M.H., Nagashima, K., Murayama, M., 2019. A 5.3-million-year history of monsoonal precipitation in northwestern Australia. *Geophys. Res. Lett.* 2019GL083035. <https://doi.org/10.1029/2019GL083035>.
- Takahashi, K., Okada, H., 2000. The paleoceanography for the last 30,000 years in the southeastern Indian Ocean by means of calcareous nannofossils. *Mar. Micropaleontol.* 40, 83–103. [https://doi.org/10.1016/S0377-8398\(00\)00033-5](https://doi.org/10.1016/S0377-8398(00)00033-5).
- Thompson, P.A., Wild-Allen, K., Lourey, M., Rousseaux, C., Waite, A.M., Feng, M., Beckley, L.E., 2011. Nutrients in an oligotrophic boundary current: evidence of a new role for the Leeuwin Current. *Prog. Oceanogr.* 91, 345–359. <https://doi.org/10.1016/j.pocean.2011.02.011>.
- Tierney, J.E., Tingley, M.P., 2014. A Bayesian, spatially-varying calibration model for the TEX86 proxy. *Geochim. Cosmochim. Acta* 127, 83–106. <https://doi.org/10.1016/j.gca.2013.11.026>.
- Unrein, F., Gasol, J.M., Not, F., Forn, I., Massana, R., 2014. Mixotrophic haptophytes are key bacterial grazers in oligotrophic coastal waters. *ISME J.* 8, 164–176. <https://doi.org/10.1038/ismej.2013.132>.
- van Sebille, E., Sprintall, J., Schwarzkopf, F.U., Gupta, Sen, A., Santoso, A., England, M.H., Biastoch, A., Böning, C.W., 2014. Pacific-to-Indian ocean connectivity: tasman leakage, Indonesian throughflow, and the role of ENSO. *J. Geophys. Res.: Oceans* 119, 1365–1382. <https://doi.org/10.1002/2013JC009525>.
- Veeh, H.H., Calvert, S.E., Price, N.B., 1974. Accumulation of uranium in sediments and phosphorites on the South West African shelf. *Mar. Chem.* 2, 189–202. [https://doi.org/10.1016/0304-4203\(74\)90014-0](https://doi.org/10.1016/0304-4203(74)90014-0).
- Veeh, H.H., McCorkle, D.C., Heggie, D.T., 2000. Glacial/interglacial variations of sedimentation on the West Australian continental margin: constraints from excess 230Th. *Mar. Geol.* 166, 11–30. [https://doi.org/10.1016/S0025-3227\(00\)00011-6](https://doi.org/10.1016/S0025-3227(00)00011-6).
- Waite, A.M., Pesant, S., Griffin, D.A., Thompson, P.A., Holl, C.M., 2007a. Oceanography, primary production and dissolved inorganic nitrogen uptake in two Leeuwin Current eddies. *Deep-Sea Res. Pt. II* 54, 981–1002. <https://doi.org/10.1016/j.dsr2.2007.03.001>.
- Waite, A.M., Thompson, P.A., Pesant, S., Feng, M., Beckley, L.E., Domingues, C.M., Gaughan, D., Hanson, C.E., Holl, C.M., Koslow, T., Meuleners, M., Montoya, J.P.,

- Moore, T., Muhling, B.A., Paterson, H., Rennie, S., Strzelecki, J., Twomey, L., 2007b. The Leeuwin Current and its eddies: an introductory overview. *Deep-Sea Res. Pt. II* 54, 789–796. <https://doi.org/10.1016/j.dsr2.2006.12.008>.
- Wijeratne, S., Pattiaratchi, C., Proctor, R., 2018. Estimates of surface and subsurface boundary current transport around Australia. *J. Geophys. Res.: Oceans* 123, 3444–3466. <https://doi.org/10.1029/2017JC013221>.
- Wijffels, S.E., Meyers, G., Godfrey, J.S., 2008. A 20-yr average of the Indonesian throughflow: regional currents and the interbasin exchange. *J. Phys. Oceanogr.* 38, 1965–1978. <https://doi.org/10.1175/2008JPO3987.1>.
- Williams, A., Althaus, F., Dunstan, P.K., Poore, G.C.B., Bax, N.J., Kloser, R.J., McEnnulty, F.R., 2010. Scales of habitat heterogeneity and megabenthos biodiversity on an extensive Australian continental margin (100–1100 m depths). *Mar. Ecol.* 31, 222–236. <https://doi.org/10.1111/j.1439-0485.2009.00355.x>.
- Windler, G., Tierney, J.E., Di Nezio, P.N., Gibson, K., Thunell, R., 2019. Shelf exposure influence on Indo-Pacific Warm Pool climate for the last 450,000 years. *Earth Planet Sci. Lett.* 516, 66–76.
- Woo, M., Pattiaratchi, C., 2008. Hydrography and water masses off the western Australian coast. *Deep-Sea Res. Pt. I* 55, 1090–1104. <https://doi.org/10.1016/j.dsr.2008.05.005>.
- Yamada, M., Wang, Z.-L., Kato, Y., 2006. Precipitation of authigenic uranium in suboxic continental margin sediments from the Okinawa Trough. *Estuar. Coast Shelf Sci.* 66, 570–579. <https://doi.org/10.1016/j.ecss.2005.11.002>.
- Young, J.R., Bergen, J., Bown, P., Burnett, J., Fiorentino, A., Jordan, R., Kleijne, A., Niel, B., Romein, A., Salis, K., 1997. Guidelines for coccolith and calcareous nannofossil terminology. *Paleontology* 40 (4), 875–912.
- Young, J.R., 1998. Neogene. In: Bown, P.R. (Ed.), *Calcareous Nannofossil Biostratigraphy*, first ed. Chapman & Hall, Cambridge, pp. 225–265. [https://doi.org/10.1007/978-94-011-4902-0\\_8](https://doi.org/10.1007/978-94-011-4902-0_8).
- Retrieved from. In: Young, J.R., Bown, P.R., Lees, J.A. (Eds.), 2014. *Nannotax 3*. <http://www.mikrotax.org/Nannotax3/>.
- You, Y., 1998. Intermediate water circulation and ventilation of the Indian Ocean derived from water-mass contributions. *J. Mar. Res.* <https://doi.org/10.1357/002224098765173455>.